nature research

https://doi.org/10.1038/s41560-020-00720-6

Supplementary information

Hydrogen production via microwave-induced water splitting at low temperature

In the format provided by the authors and unedited

Hydrogen production via microwave-induced water splitting at low temperature

J.M. Serra[1]*, J.F. Borras-Morell[1,2], B. Garcia-Baños[2], M. Balaguer[1], P. Plaza-Gonzalez[2], J. Santos-Blasco[1], D. Catalán-Martínez[1], L. Navarrete[1,2] and J.M. Catala-Civera[2]*

[1]Instituto de Tecnología Química, Universitat Politècnica de València-Consejo Superior de Investigaciones Científicas, Avenida de los Naranjos s/n, Valencia,46022, Spain.

[2]Instituto ITACA, Universitat Politècnica de València, Camino de Vera, Valencia, 46022, Spain.

*Correspondence to: jmserra@itq.upv.es, jmcatala@dcom.upv.es.

This Supplement contains:

Supplementary Figures 1 to 23
Supplementary Notes 1 to 14
Supplementary Tables 1 to 8
Supplementary Reference List

Supplementary Figures

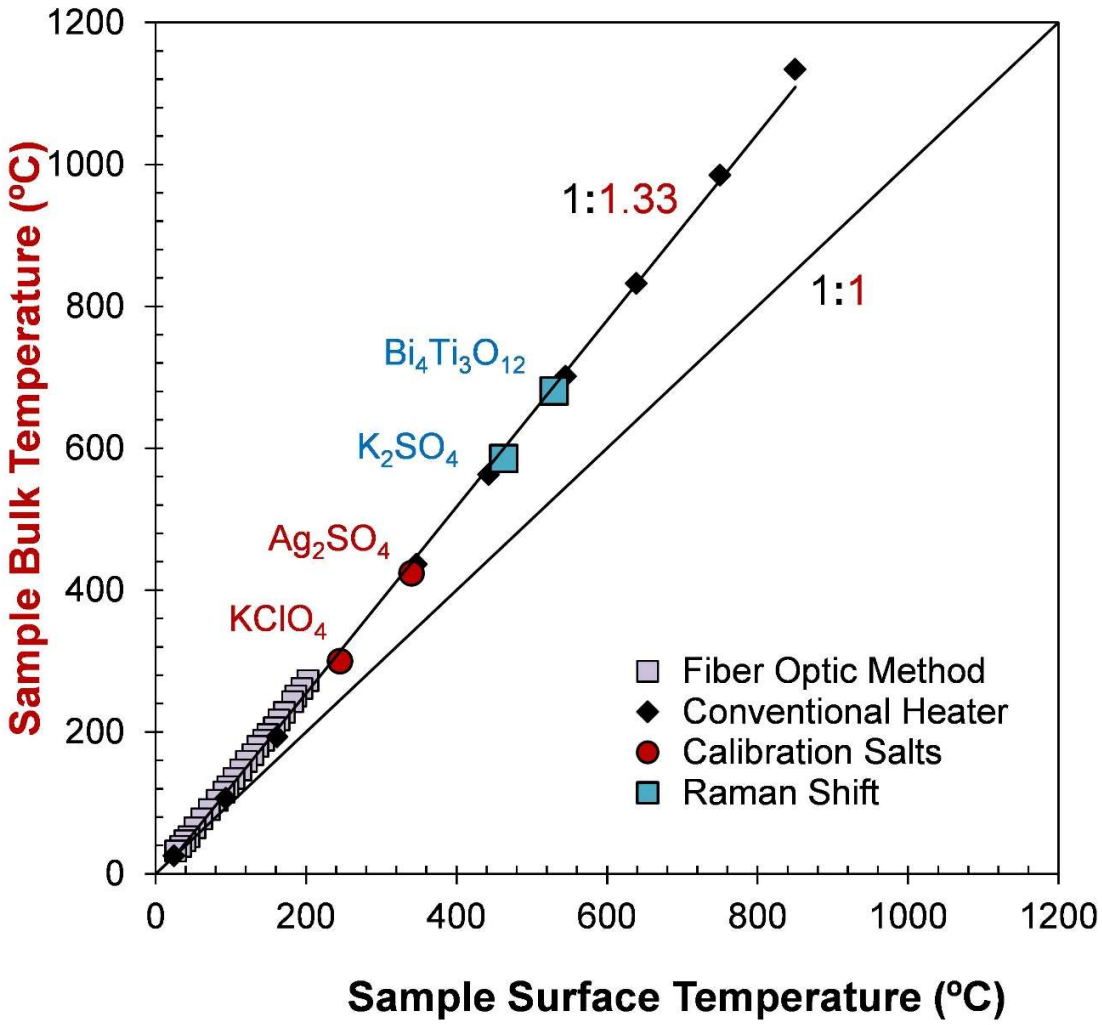

Supplementary Figure 1. Bulk temperature calibration. Calibration of bulk temperature of samples as a function of the measured surface temperature by the IR pyrometer in the microwave cavity. Microwave power adjusted at an approximate rate of 1-10 ºC·s^{-1}.

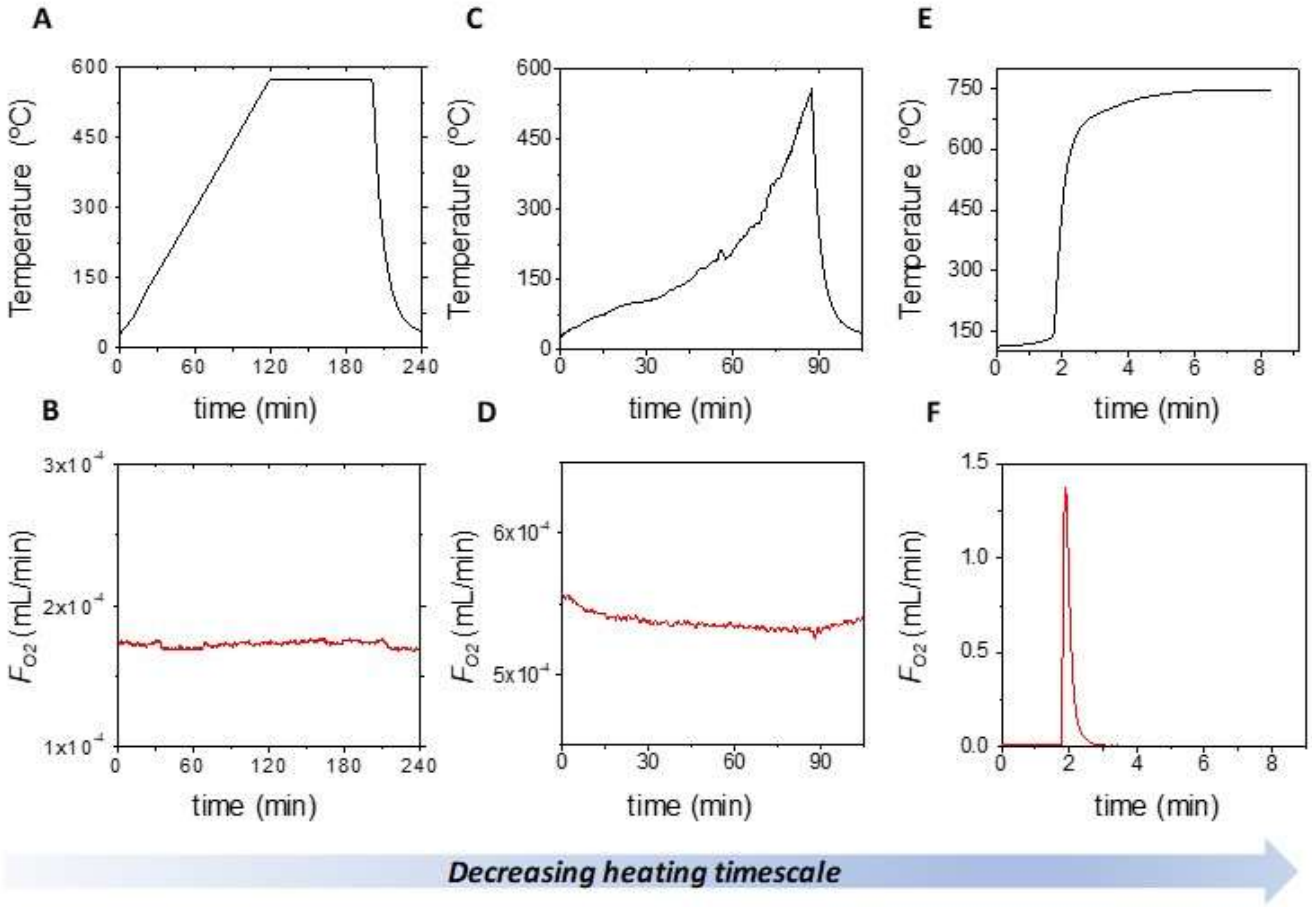

Supplementary Figure 2. Comparison of ceramic heating methods and oxygen release. After a purging heating cycle in air, CGO sintered at 1400 ºC was heated up. **a, b,** Conventional heating at a rate of 10 ºC·min^{-1} up to 600 ºC in Ar. **c, d,** Heating below microwave power threshold, P_{th}, in N_2. **e, f,** Heating upon P_{th} in N_2. The oxygen yield was monitored by following the m/z = 32 and 16 amu by mass spectrometry. The experiments were performed in a 100 mL·min^{-1} (STP) gas flow**.**

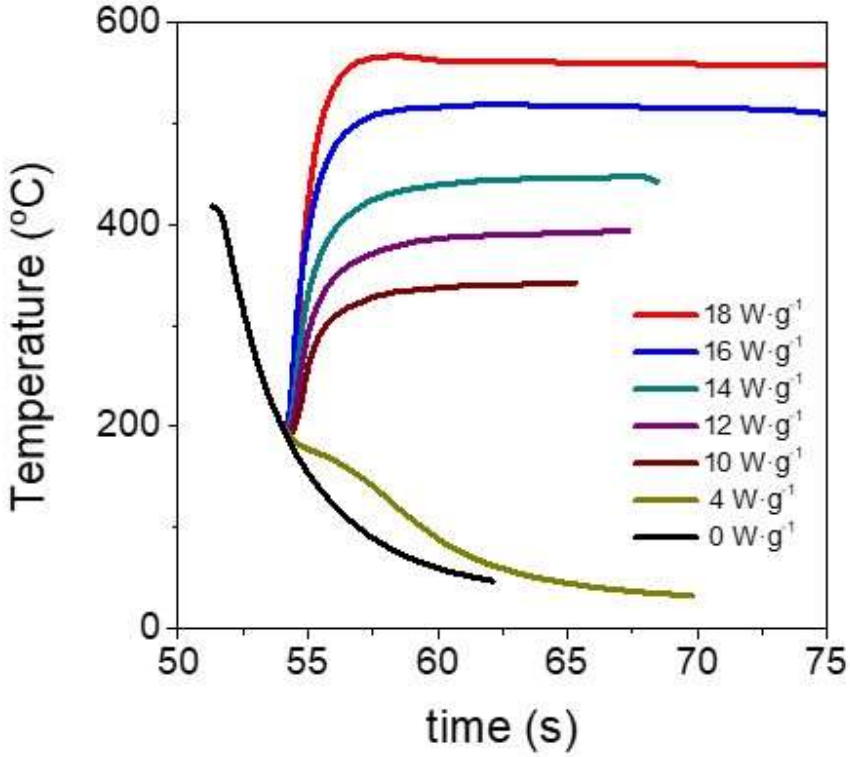

Supplementary Figure 3. Effects of microwave power intensity on the heating dynamics. The evolution of temperature was analyzed by radiating at constant absorbed power a CGO sample initially set at 200 ºC (T>T_{ind}) in an oxidizing atmosphere. Whereas a large sharp temperature step rise is found for power rates above the threshold, a very smooth damped distribution is reported otherwise (even just below the threshold) without any sign of oxygen release. The very dissimilar heating behavior can only be ascribed to the microwave triggered activation of the material reduction.

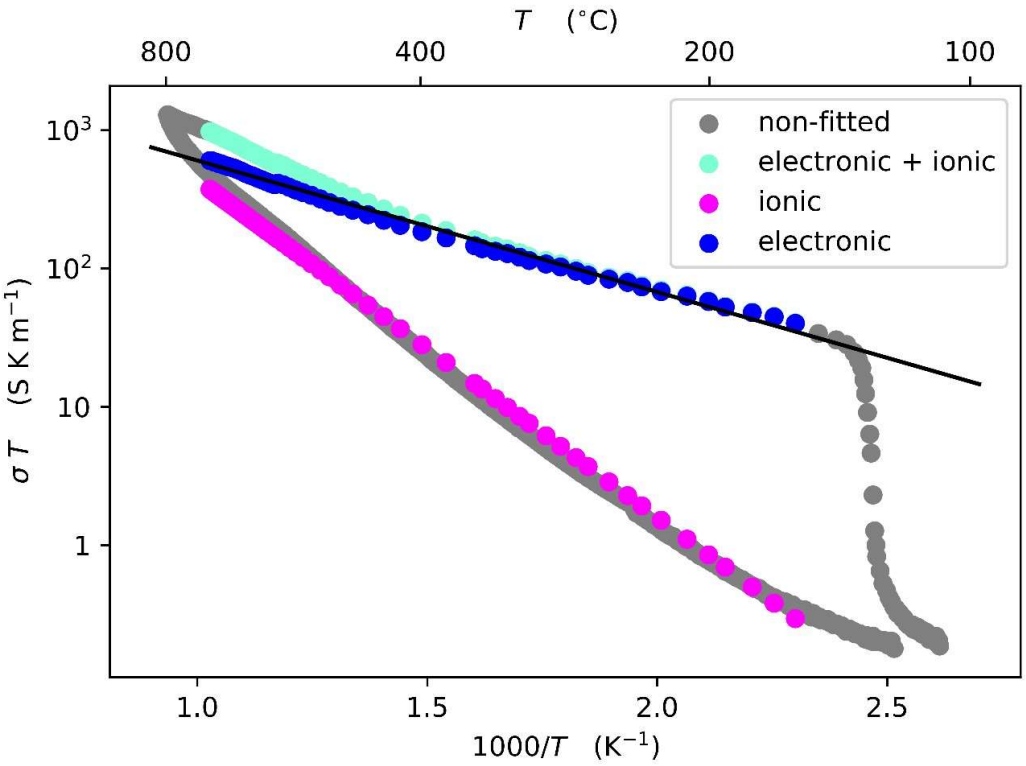

Supplementary Figure 4. Conductivity decomposition during microwave-assisted heating. The microwave irradiation of a CGO sample unveils the very characteristic conductivity abrupt raise after reaching T_{ind} for a supplied microwave power above the reduction threshold. Further conductivity rise is decomposed as the sum of its thermal activated electronic and ionic contributions during the material heating up.

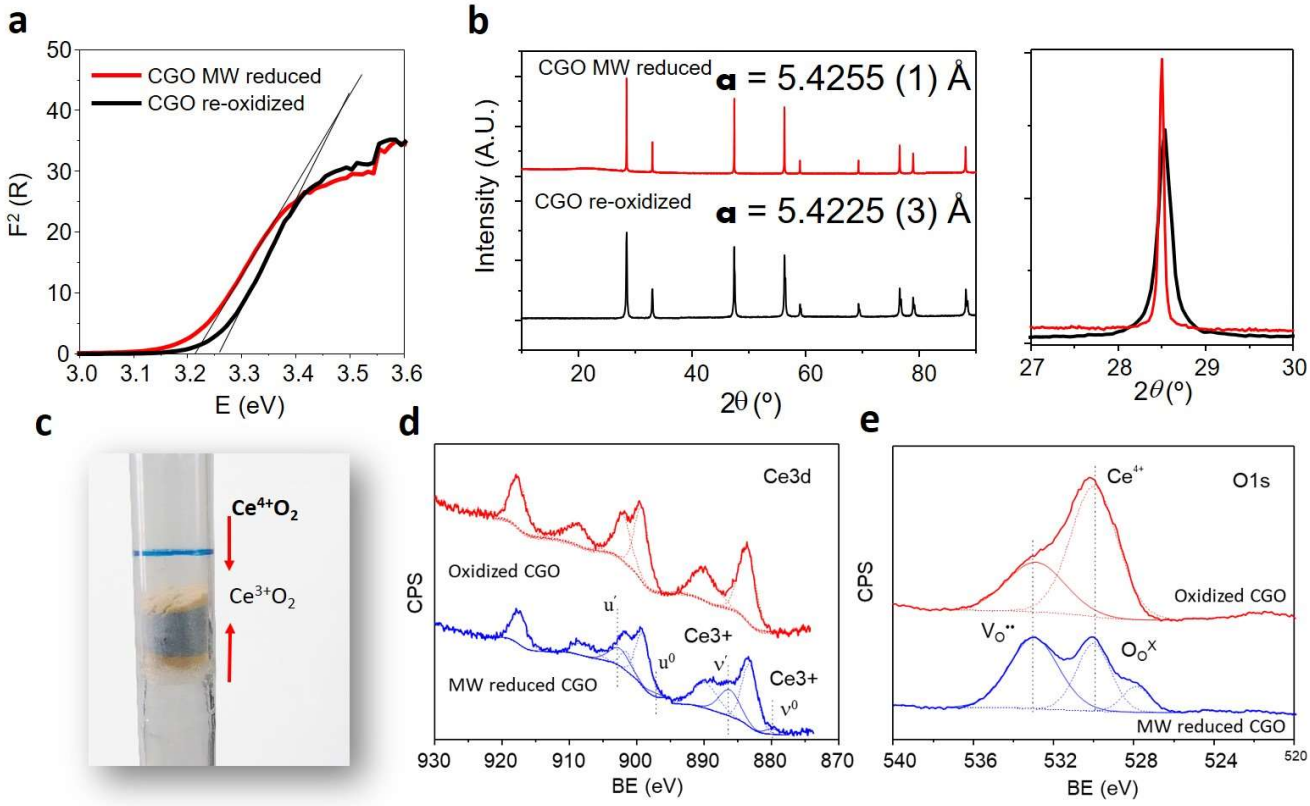

Supplementary Figure 5. Structure and surface characterization. a, UV-vis $F^2(R)$ absorption spectra versus the photon energy for CGO after microwave exposure and further re-oxidation in air allows extracting energy gaps of 3.20 eV and 3.26 eV, respectively. The microwave irradiation reduces the band gap energy and introduces new electronic states within, suggesting that reduction increases electronic conductivity. microwave reduction at constant absorbed power (30 $W \cdot g^{-1}$). **b,** The XRD patterns of the CGO sample after the microwave treatment until 400 °C in Ar are shifted to lower angles regarding the CGO re-oxidized in air. In the right, a zoom of (1 1 1) peak. Cell parameter decreases from 5.4255 Å for the microwave reduced CGO to 5.4225 Å after air re-oxidation. **c,** The reduction of CGO is detected macroscopically by the change in color of the powder, from blue color of the reduced CGO to yellow as it oxidizes in contact with ambient air. **d,** XPS Ce3d line shows peaks at 880.0 eV (ν^0) and 886.3 eV (ν') attributed to Ce^{3+}. Doublet at 902.8 (u') and 897.2 (u^0) are clearly observed in the microwave irradiated CGO sample, while absent in the thermal treated sample. A 27% Ce^{3+}/Ce^{4+} surface ratio is estimated on the microwave irradiated sample. **e,** XPS O1s lines revealed the increase of surface oxygen vacancies concentration after irradiation by the growth of the 532.9 eV O1s peak compared to the 530.0 eV peak. The high BE peak has been ascribed to defect sites, i.e. oxygen vacancies or CO_2-contamination or hydroxyl groups, while the low BE peak corresponds to lattice oxygen in the fluorite structure of CGO. The amount of vacancies i.e. $V_O^{\cdot\cdot}/O_O^X$ increases from 0.47 to 1.5 (microwave irradiated sample).

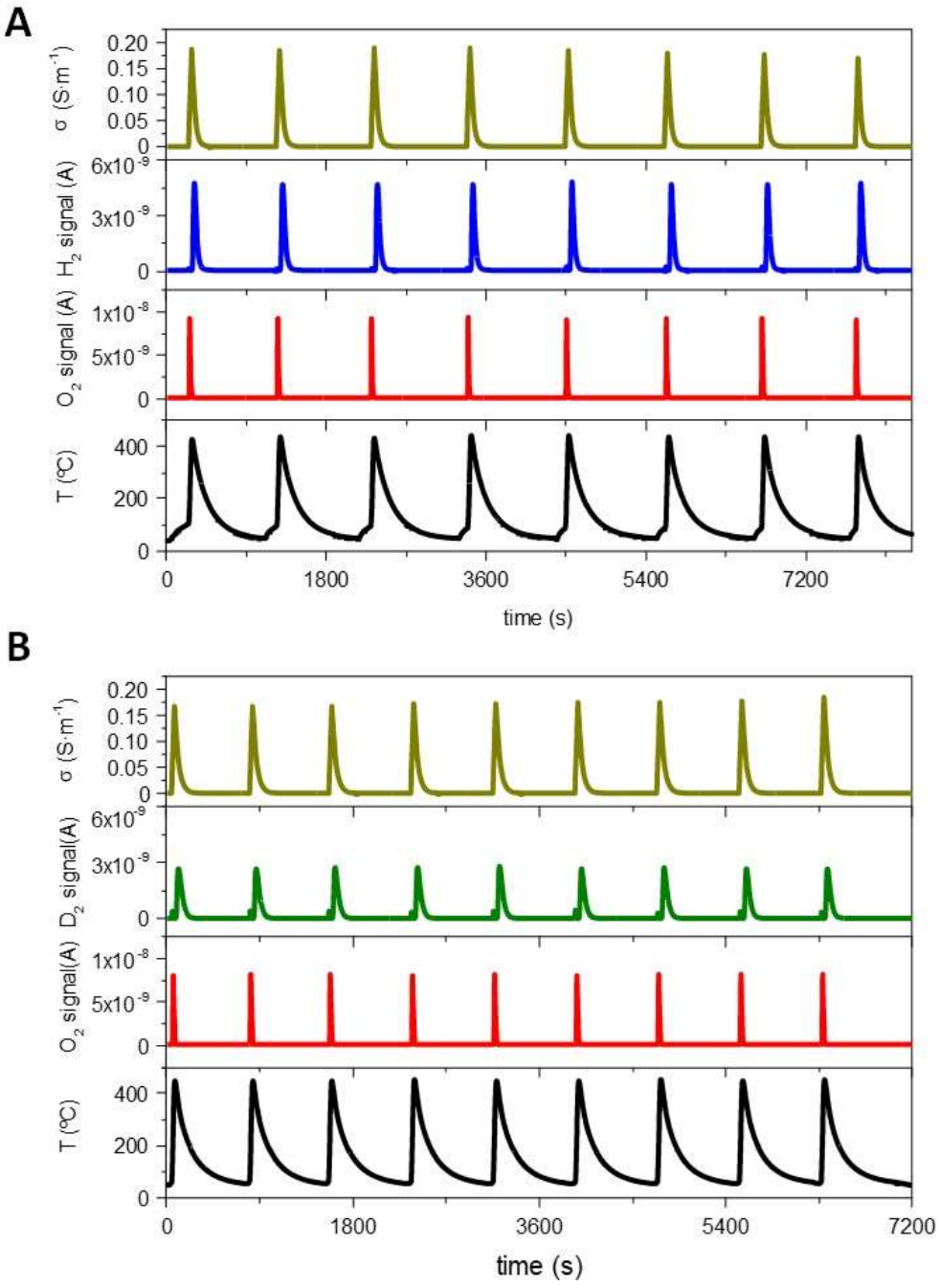

Supplementary Figure 6. Deoxygenation of H_2O and D_2O to produce H_2 and D_2. a.c. electric conductivity, temperature, O_2-assigned MS signal and production of **a,** H_2 from H_2O reduction and **b,** D_2 from D_2O reduction. The yield of O_2 occurs simultaneously with the rise in temperature and conductivity while the production of H_2 or D_2 starts upon microwave switching-off: H_2O/D_2O splitting occurs through the re-oxidation of CGO material. The N_2 gas flow was saturated with H_2O or D_2O at 25 °C (3% H_2O/D_2O in N_2).

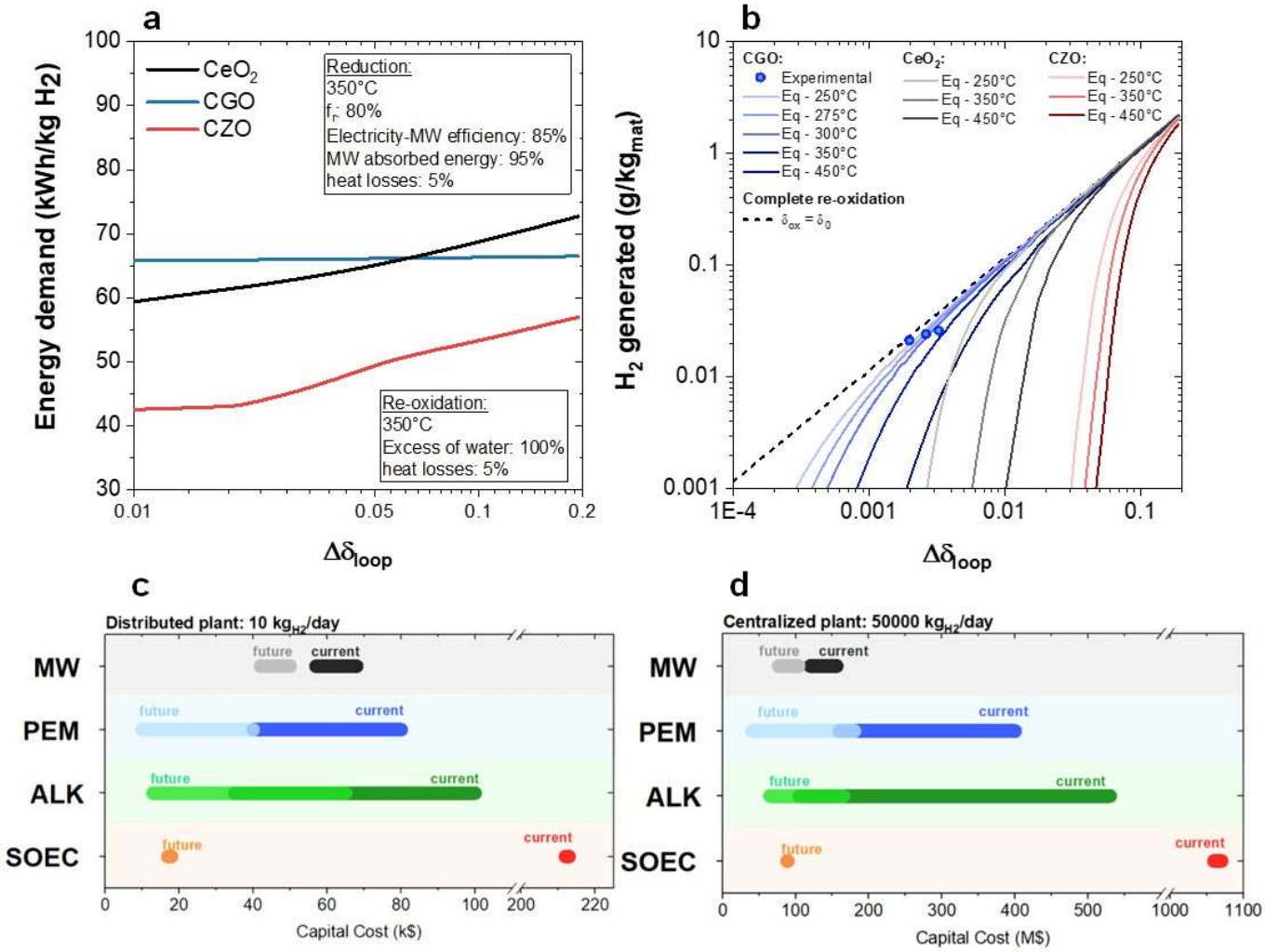

Supplementary Figure 7. Thermodynamic modelling evaluation of the loop process and capital cost comparison of H_2 production technologies. a, Effect of the oxygen vacancy fraction achieved in the reduction on the H_2 energy demand. BoP energy not considered. Reduction and re-oxidation at 350 °C, f_r=0.8, Heat losses: 5%, Non-absorbed MW: 5%. **b**, Comparison between the H_2 generated in the re-oxidation of the experimental test and the equilibrium reached at different temperatures depending on the oxygen vacancy fraction difference between the initial state of the material and the reduced state, $\Delta\delta_{loop}=(2-\delta_0)-(2-\delta_r)$. **c**, Comparison of the capital cost for a distributed plant of 10 kg/day of H_2 using microwave-assisted process and PEM, alkaline (ALK) and SOEC water-electrolysis technologies. **d**, Comparison of the capital cost for a centralized plant of 50000 kg/day of H_2 using microwave-assisted process and PEM, alkaline (ALK) and SOEC water-electrolysis technologies.

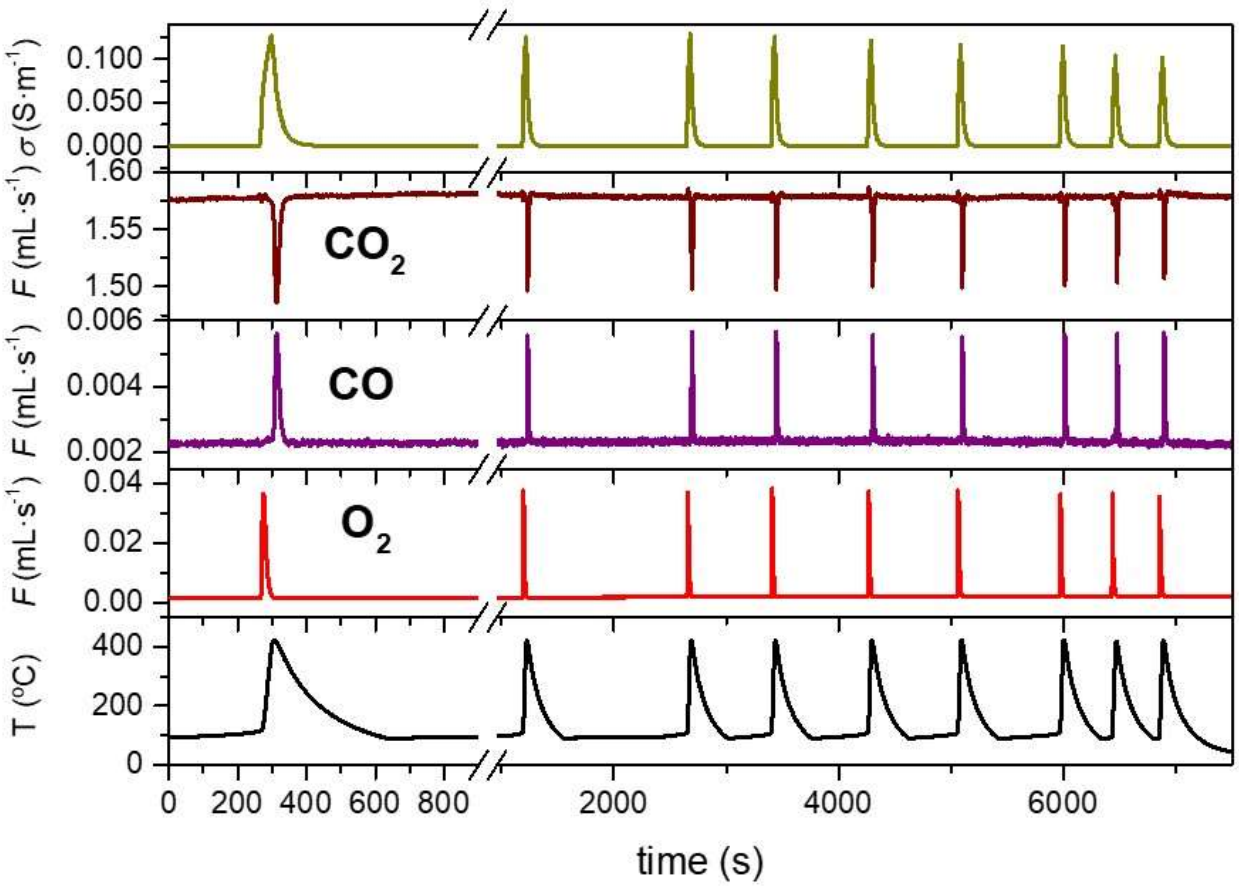

Supplementary Figure 8. Deoxygenation of CO_2. Conductivity, temperature, O_2, CO_2 and production of CO via CO_2 de-oxygenation through the re-oxidation of CGO lattice. A gas flow of a calibrated gas mixture (15% CO_2 in Ar) was used in the whole experiment. Microwave Power ~35 $W \cdot g^{-1}$.

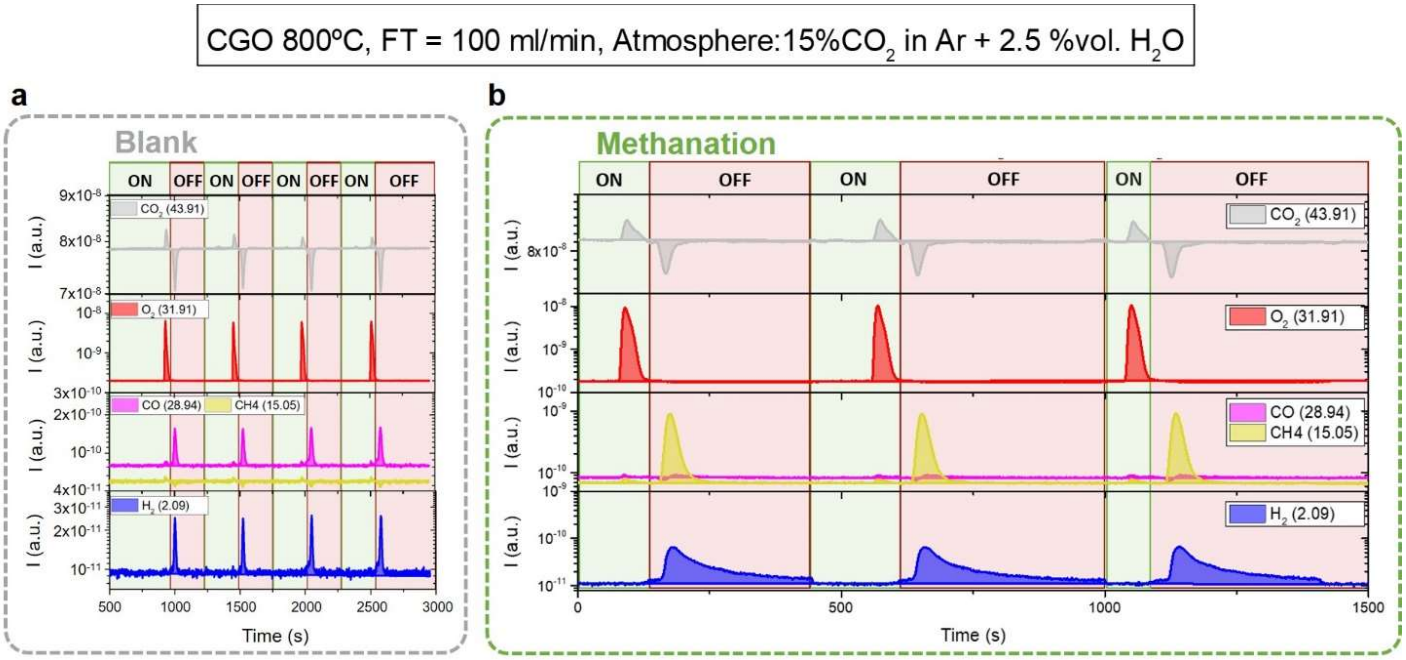

Supplementary Figure 9. CO/CO_2 hydrogenation. Mass spectrometer signal for the target gases, CO_2 (m = 43.91), O_2 (m = 31.91), CO (m = 28.94), CH_4 (m = 15.05) and H_2 (m = 2.09), in the CO and CO_2 hydrogenation reaction. **a,** Ion current signal for the gases in the microwave cavity outlet stream, for the consecutive cycles of CGO microwave radiation. The cavity is feed with a total flow of 100 ml·min^{-1} and it is comprised of 15% of CO_2, 2.5 % vol. of H_2O and rest is Ar. **b,** Analysis of the methanation reaction outlet gases, after the reaction of the H_2, CO and CO_2 obtained in the microwave cavity over the Ru-based catalyst at 350 ºC. In each cycle, an initial O_2 and CO_2 release was observed, afterwards the signal of CH_4 and H_2 increased due to reductive process coupled with the catalytic methanation reaction. Several catalytic reactions are suggested for the CH_4 formation from CO_2 or CO. In addition, it has been suggested that CO acts as intermediate in the CO_2 hydrogenation. Thus, CO, generated in the microwave cavity, and CO_2 react with the H_2, produced from the CGO oxidation, over Ru-catalyst. The different possible reactions are $CO_2+4H_2 \leftrightarrow CH_4+2H_2O$, $CO_2+H_2 \leftrightarrow CO+H_2O$, $CO+3H_2 \leftrightarrow CH_4+H_2O$ and $CO+H_2O \leftrightarrow CO_2+H_2$. The CO generated in the microwave cavity and the CO_2 not reduced in the cavity react with the H_2 produced in the CGO oxidation. CH_4 is formed and some H_2 is also observed in the mass spectrometer signal. This H_2 can be related with the Water Gas Shift Reaction Eq. (19), which is favored at the operation conditions (350 °C).

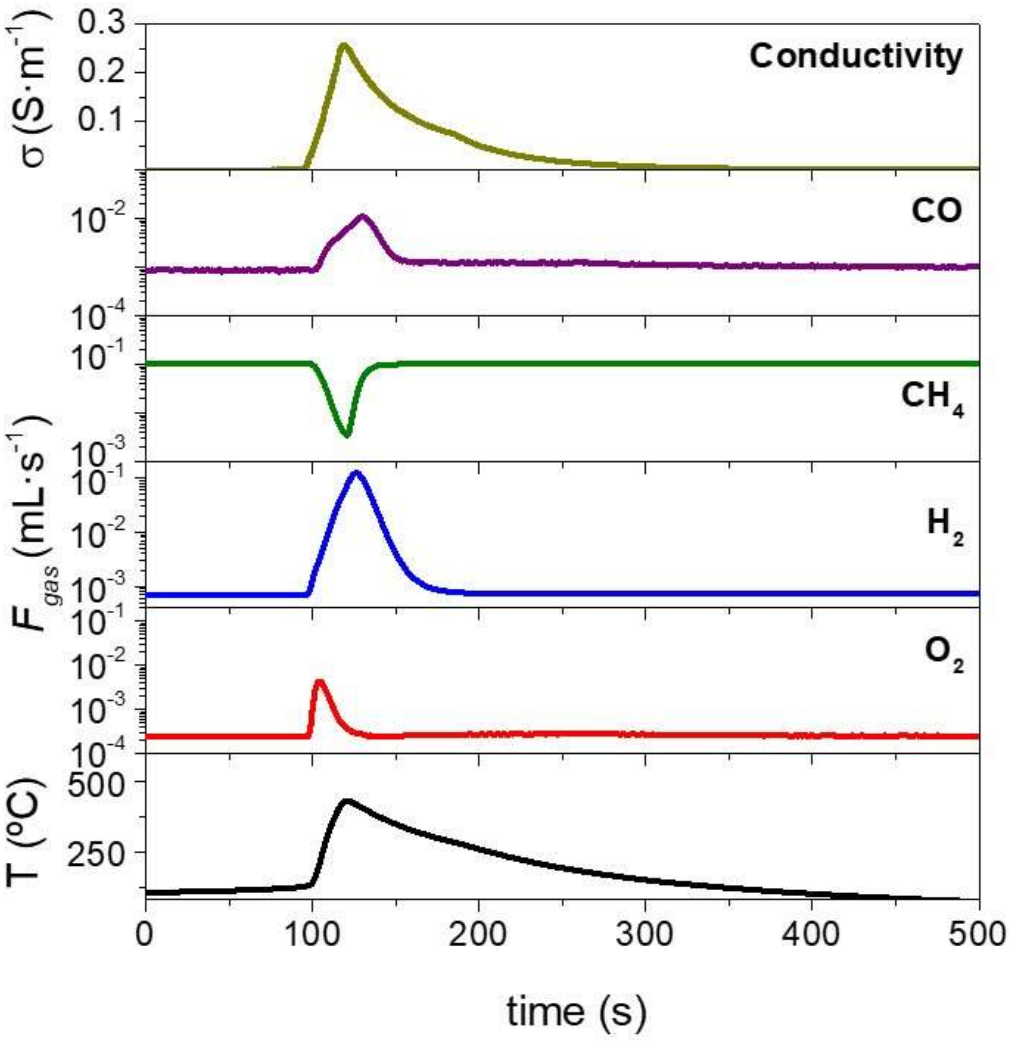

Supplementary Figure 10. Microwave electrocatalysis. The utilization of CH_4 to produce basic chemicals in the industry relies upon its transformation into syngas. Diverse H_2/CO ratios are obtained depending on the selected synthesis route (Dry reforming: $CH_4+CO_2 \rightarrow 2H_2+2CO$, Steam reforming: $CH_4+H_2O \rightarrow 3H_2+CO$ and Partial Oxidation: $CH_4+1/2O_2 \rightarrow 2H_2+CO$). The syngas is widely employed in the chemical industry for the Fischer-Tropsch methanol synthesis. The most suitable ratio of H_2 to CO for those reactions is 2, and the Partial Oxidation of Methane is the only one that fulfils that condition and does not need to be adjusted with additional gases. For the total conversion of methane with high selectivity to CO, high temperatures (>750 °C) are required. In order to reduce the operation temperature different catalyst can be employed. Transition metals like Ni, Co and Fe, perovskites or noble metals are widely studied. One of the main challenges for the Catalytic Partial Oxidation of Methane is the development of a selective and stable catalyst for the operation temperature decrease. As a result, carrying out the POM reaction by the contactless microwave technique, with the possibility of using different oxides, opens a new field of research. Conductivity, temperature and gas evolution during the partial oxidation of methane through the reduction of CGO lattice for syngas production are represented here.

Supplementary Notes

Supplementary Note 1: Microwave irradiation of samples

Experimental setup for microwave redox activation was based on the microwave system described in a previous work[1] with specific modifications to operate in continuous flow under different gas atmospheres. The microwave cylindrical cavity (104.92 mm in diameter, 85 mm in height) was designed to irradiate samples of solid materials and perform simultaneous *in situ* measurements of the a.c. conductivity.

The irradiation of solid materials (in a tubular volume of 9.8 mm in diameter and 15 mm in height) was realized through the application of microwave power in the cylindrical Transversal Electric mode TE_{111} around the ISM (Industrial, Scientific and Medical) frequency of 2.45 GHz.

The cavity has open cut-off holes in the upper, lower and lateral walls for insertion of the pass-through tubular quartz reactor containing the sample, location of antennas for coupling of microwaves and process monitoring. A mass spectrometer apparatus (Omnistar Balzers) was connected to the output of the tubular quartz reactor to measure the composition of the off-gas during the experiments.

Fig. 1 (in main text) illustrates the microwave setup including the theoretical TE_{111} electromagnetic field distribution in the resonant microwave cavity in comparison to the sample size[2]. This selection ensures an intense and uniform processing of the materials inside the reactor (E-field of TE_{111} mode, also included in Supplementary Figure 11a).

The setup for microwave irradiation was completed by a 120 W solid-state microwave amplifier (RCA2026U50, RFcore Ltd. from 2.2 to 2.6 GHz) driven by the oscillator and receiver of a network analyser (Rohde & Schwarz ZVRE) and a microwave control system.

The microwave control system, located next to the irradiation source (amplifier) in the experimental setup, made use of a variable coupling device (coaxial probe with variable penetration) and a double directional coupler (Meca Electronics, model 722-40-1.950 W) to adjust and measure the reflected signals from the microwave cavity as a function of frequency and temperature, in order to provide the desired level of heating rate to the sample (see next Supplementary Notes). This configuration enables to reach temperatures higher than 1000 ºC in the sample under different gas atmospheres.

To determine the bulk temperature of the sample, the surface temperature of the quartz reactor was measured by an IR pyrometer (Optris CT-Laser LT), with extensive calibration procedures including measurements of fibre optic (FO) sensors placed in contact with the material's body (Supplementary Note 3).

Supplementary Note 2: a.c. conductivity set up

A microwave source and receiver of a low power vector network analyzer (Hewlett Packard HP8720E) were coupled to the microwave cavity through the SubMiniature version A (SMA) connector placed at the bottom wall of the cavity, for measurements of microwave a.c. conductivity for the tested samples. The cavity resonance response of the electromagnetic cylindrical mode

TM_{010}, employed for conductivity calculations (Supplementary Note 5). The continuous sweep of the generator frequencies from 1.9 GHz to 2.2 GHz and received signals allowed to extract two different microwave sources at slightly different microwave frequencies and a high isolation cross-coupling filter[1] were used for the microwave heating and simultaneous conductivity measurements without interferences. Supplementary Figure 11 shows the theoretical electromagnetic amplitude distributions of both cylindrical modes in the empty cavity. Both E-field patterns have the maximum magnitude at the cavity center. The heating TE_{111} mode E-field vector mode is perpendicular to the cavity axis whereas the measuring TM_{010} mode E-field vector is parallel to the cavity axis[2]. A detailed view of the TE_{111} mode E-field with the quartz reactor filled with the CGO sample is depicted in Supplementary Figure 12a. The E-field distribution in the cavity reactor and bed body was simulated with Quickwave 3D electromagnetic simulator (QW3D). QW3D allows to define the specific geometry and run a FDTD analysis with a specific sinusoidal excitation to calculate the E-field distribution in the cavity. Supplementary Figure 12b shows how the intensity of the electric field inside the catalyst bed remains moderately invariant along the sample volume.

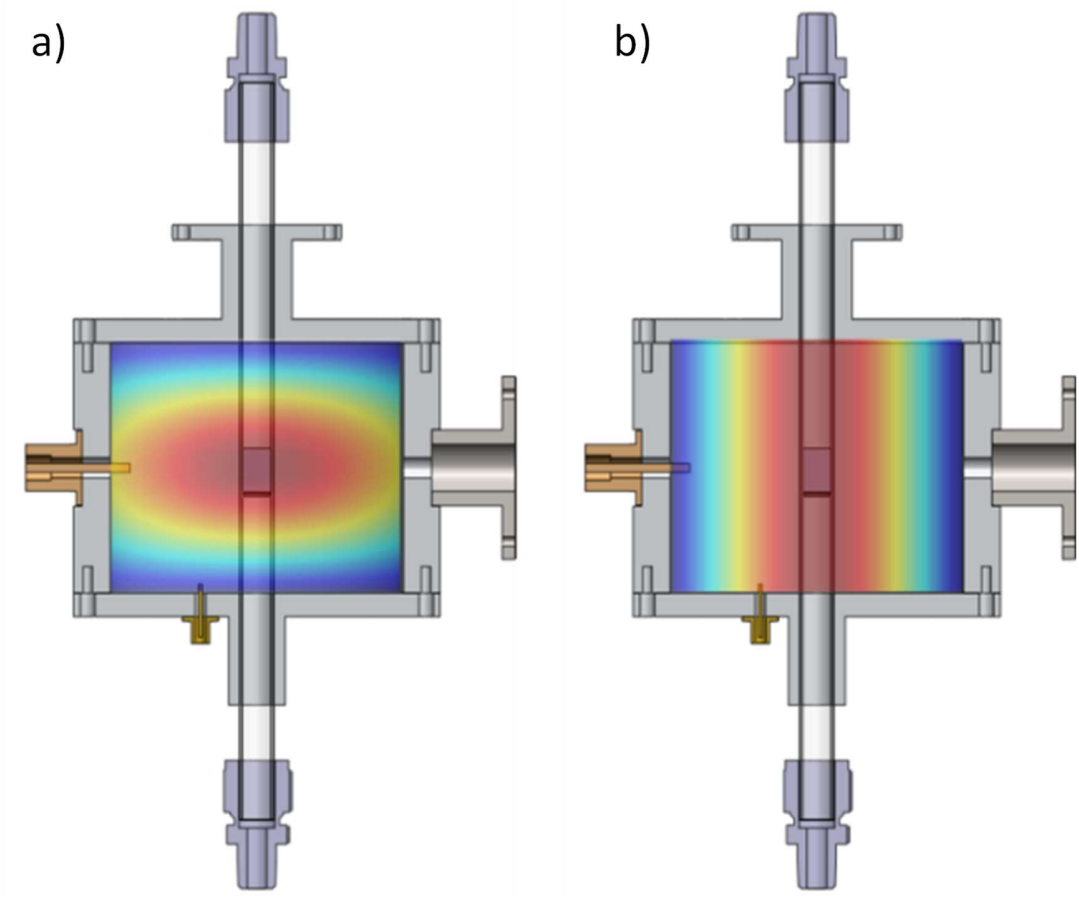

Supplementary Figure 11. Theoretical E-field distribution of cylindrical modes in the empty microwave cavity: **a,** the heating TE_{111} mode with E-field vector mode perpendicular to the cavity axis and **b,** the measuring TM_{010} mode E-field vector parallel to the cavity axis.

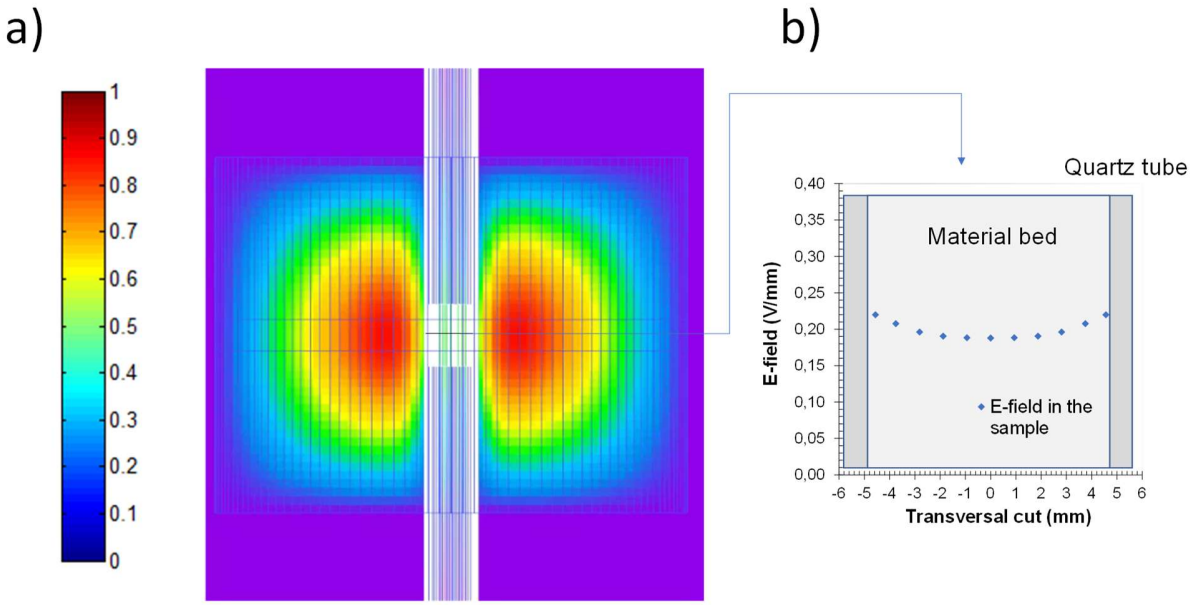

Supplementary Figure 12. a, simulated E-field distribution in the microwave cavity with the quartz reactor filled with CGO (E-field normalized to 1 in the microwave cavity). **b,** Simulated transversal cut of the E-field across the CGO bed.

Supplementary Note 3: Experimental setup for measurement using conventional heating

An electric resistance furnace was employed for a.c. conductivity measurements under conventional heating and it was located above the cylindrical cavity[3]. The a.c. conductivity measurements were conducted in three different steps. Firstly, cylindrical samples, with a dimension of 9.8 mm diameter and 15 mm height of the particulate materials, were prepared and placed on a quartz frit membrane located in a long tubular quartz reactor. The quartz reactor was heated in the conventional furnace outside the cavity until reaching the desired temperature. Secondly, the reactor containing the sample was moved to the cavity for the conductivity measurements in order to characterize the sample with the same setup as described in Supplementary Note 2. Finally, the quartz reactor was rapidly moved back to the furnace to continue with the heating process. Supplementary Figure 13 shows the drawing of the additional setup placed on the top of the microwave cavity for resistive heating of the samples.

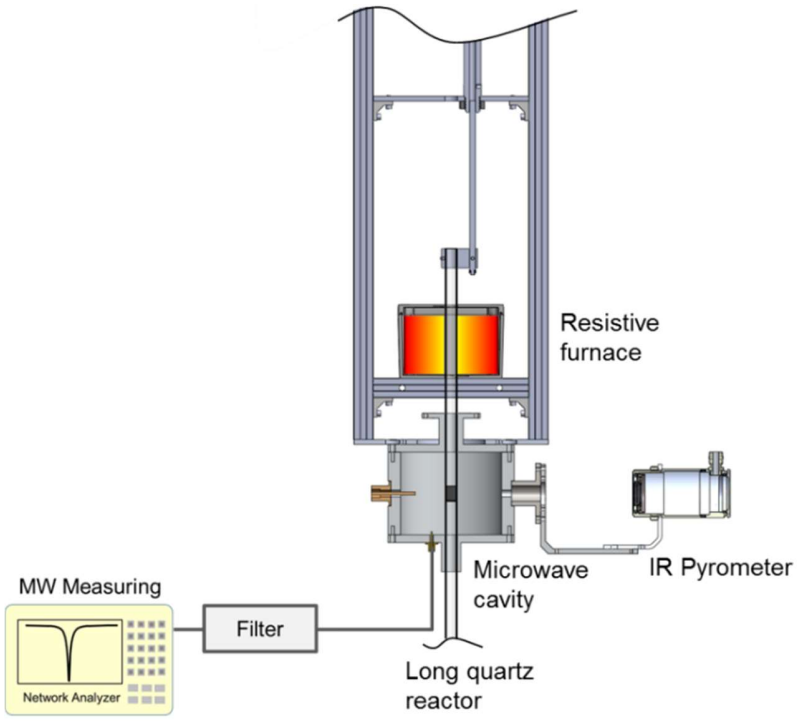

Supplementary Figure 13. Experimental setup for conventional heating of samples and conductivity measurements.

Supplementary Note 4: Microwave heat generation and control

The microwave power absorbed by the sample was adjusted by fixing the coupling device to a specific penetration and dynamically selecting the frequency sweeps of the microwave source around the frequency peak of the cavity, as the heating of the sample was progressing.

The microwave power absorbed, $P_{abs}(f_i)$, in the microwave reactor was calculated as the power delivered by the generator (output of microwave amplifier P) and the reflected signals (S_{11}) modified by the coupling device, for each specific frequency f_i selected from the source oscillator. This relation is given by the equation:

$$P_{abs}(f_i) = P(1 - |S_{11}(f_i)|^2), \qquad i = 1, \dots, N; \tag{1}$$

where N is the number of frequency points. Thus, the average absorbed power (P_{MW}) for a frequency sweep in the range $[f_1 < f_i < f_N]$ can be written as

$$P_{MW} = \frac{1}{N}\sum_{i=1}^{N} P_{abs}(f_i). \tag{2}$$

Then, by selecting the appropriate frequency sweeps of the microwave source around the frequency peak of the cavity (f_1 and f_N), we can provide the required level of microwave power (average microwave power) to the microwave reactor according to a desirable heating rate (K/s).

An example of this procedure is given in the following figures. Supplementary Figure 14 displays the measurement of the reflection factor (S_{11}) of the irradiation TE_{111} mode of the microwave cavity for a specific penetration of the coupling device with a coupling level close to -25 dB, when loaded with the quartz tube reactor and a sample of CGO (25 ºC). The resonant peak of the cavity can be identified around 2.451 GHz in the plot.

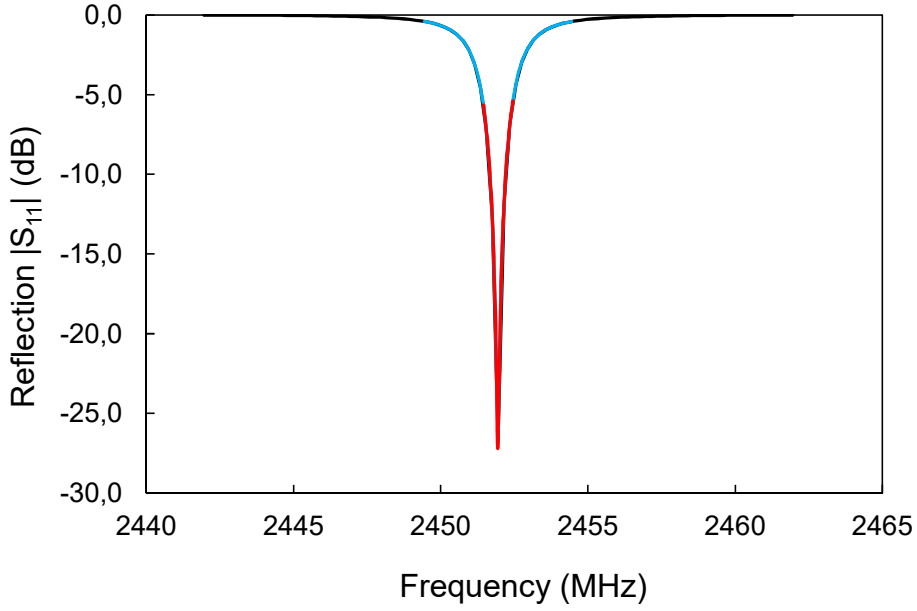

Supplementary Figure 14. Reflection factor (S_{11}) of the microwave cavity around the resonant peak of the irradiation TE_{111} mode when loaded with the quartz tube reactor and a sample of CGO (25 ºC).

For a wide frequency sweep of 20 MHz (from 2.441–2.461 GHz) around the frequency peak, the average power P_{MW} released to the microwave reactors results in 14 W, according to Eqs. (1) and (2), since the reflection factor S_{11} at frequencies far away from the resonance is very high and heat is only applied around the resonant peak in a similar shape to pulses with low duty cycle (~20%). Otherwise, for frequency sweeps of 5 MHz (from 2.449–2.454 GHz), P_{MW} increases to 48 W (duty cycle 40% due to less points with high S_{11}) and for frequency sweeps of 1 MHz around the frequency peak (from 2.451 to 2.452 GHz, red line in Supplementary Figure 14) P_{MW} results in 105 W (duty cycle 80%). Supplementary Figure 15 shows the variations of the frequency of the source and the absorbed power in the microwave reactor with processing time, according to the previously selected frequency sweep ranges. Each frequency sweep lasted 200 ms with $N = 100$ frequency points measured.

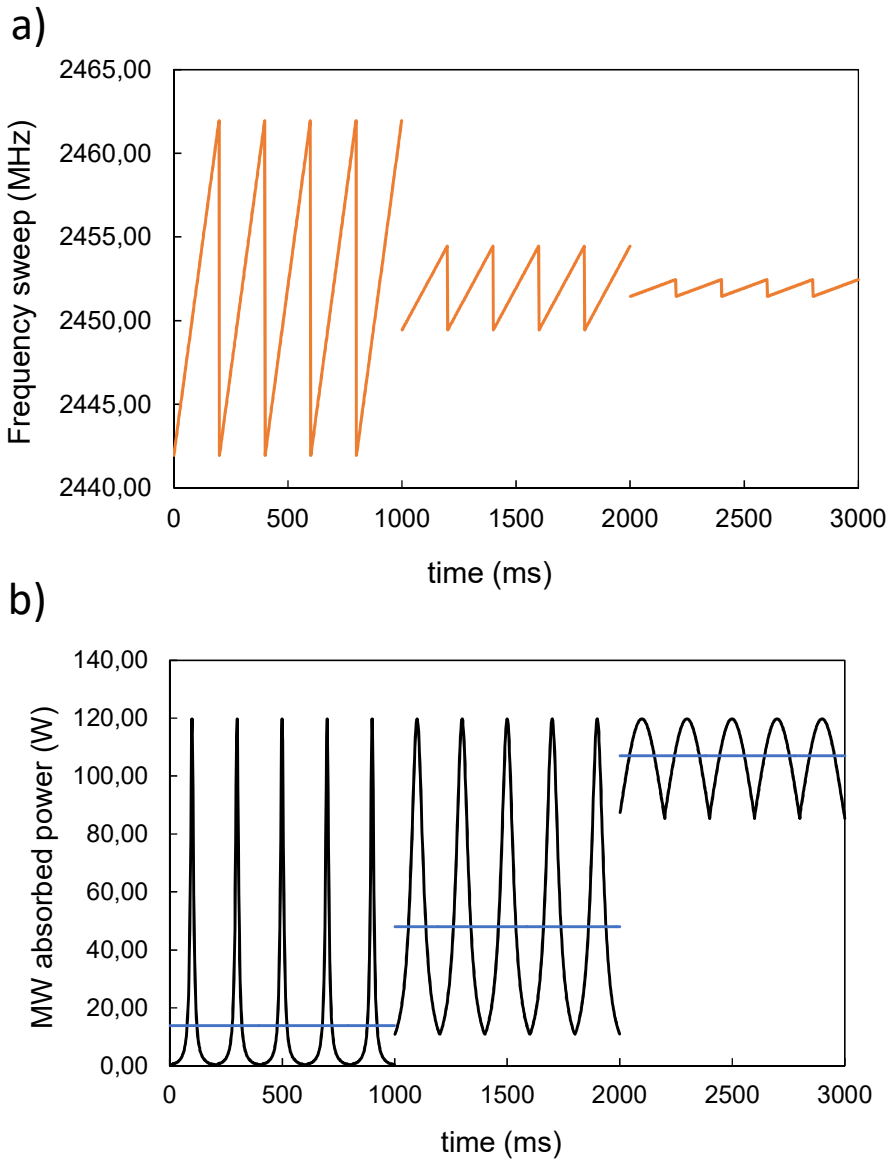

Supplementary Figure 15. a, Frequencies selected in the microwave source for irradiating the CGO sample in the cavity. **b,** Instantaneous absorbed microwave power (black) and average absorbed microwave power P_{MW} (blue) in the microwave reactor as a function of the processing time for frequency sweeps of 20 MHz, 5 MHz and 1 MHz, respectively.

The design of the microwave heating cavity and the advanced control of the microwave power supplied to the sample allowed for very high reproducibility of results, which was fundamental to overcome the poor level of performance associated to multimode instruments in small-scale experiments. Even if the microwave power is very high (1000 W) in a multimode furnace, the final power field density on the samples is rather low compared to the E-field density achieved in the described cavity.

Supplementary Note 5: a.c. conductivity measurements

The measurement of a.c. conductivity for solid materials at microwave frequencies as a function of temperature relies on the Microwave Cavity Perturbation Technique (MCPT) and allows the simultaneous measurement of permittivity and conductivity[4].

The measurement of conductivity using microwave techniques was reported previously[5]. One of the main applications of MCPT consists of measuring the fast time evolution of the conductivity of some materials excited by different sources. This technique, called TRMC (Time Resolved Microwave Conductivity), was reported[6] to measure the formation of electronic charge carriers in bulk materials induced by a short pulse of high-energy radiation (PR-TRMC, Pulse-Radiolysis Time Resolved Microwave Conductivity).

Another work[7] reported the time evolution of the complex conductivity of samples after photoexcitation with flash-photolysis Time Resolved Microwave Conductivity (fp-TRMC) experiments to study the photoconductance (free charge generation) on solution-phase samples. The same technique was applied in a microwave cavity[8] to measure the charge carrier's generation at the semiconductor/insulator interface when an external gate bias was applied (Field-induced Time-Resolved Microwave Conductivity, FI-TRMC). MCPT has also been applied to measure the temperature dependence of conductivity and permittivity of single and polycrystalline samples in a flow-through reactor with simultaneous gas-flow heating in the temperature range of 20–500 ºC[9].

In a recent paper[1], MCPT was applied in a dual-mode cavity excited by two different microwave sources to measure the temperature dependence and time evolution of permittivity (and therefore the conductivity) of materials simultaneous with the heating of the sample by high power microwaves. To our knowledge, MCPT has not been used to quantitatively determine the conductivity of ionic conductors or to monitor redox reactions as a function of temperature under microwave working conditions, as described in this paper.

The fundamental concept of the MCPT relies on the fact that the introduction of a small sample or a slight perturbation in a resonant cavity barely alters the microwave electromagnetic (EM) fields around the material. The method requires the measurement of the resonance characteristics of the microwave cavity before the insertion of the material sample to be measured, after the insertion of the empty quartz reactor inside the cavity and continuously during the microwave irradiation of the sample (and the quartz reactor) in the cavity.

Changes in the real part of the permittivity shift the resonance frequency of the cavity, $\Delta f / f$, whereas changes in the imaginary part determine variations in the microwave losses or Q-factor, $\Delta(1/2Q)$. The conductivity and permittivity of the sample are related through

$$\sigma_{AC} = \omega\varepsilon_0\varepsilon''_{eff} = \omega\varepsilon_0\varepsilon''_{\mathrm{d}} + \sigma\,, \qquad (3)$$

where σ_{AC}, ω, ε_0 and ε''_{eff} represent, respectively, the microwave conductivity, the angular frequency of the microwave signal, the vacuum permittivity and the imaginary part of the permittivity. The latter term, that account for the system's energy loss, can be further split into two contributions: the real component of the conductivity, σ, and the bound charge and dipole relaxation contribution to the imaginary part of permittivity, $\varepsilon''_{\mathrm{d}}$. However, these two loss mechanisms cannot

be distinguished with microwave measurements and the contribution of each term on the overall conductivity specifically depends on the material composition.
The continuous measurement of the resonant frequency and Q-factor of the cavity, from the second microwave system coupled to the bottom of the cavity (measurement mode TM_{010}), determines the frequency shift of the cavity. The change in frequency and Q-factor are described, respectively, using the following equations[1],

$$\frac{\Delta f}{f} = \frac{f_{uts} - f_{ut}}{f_{uts}}, \tag{4}$$

$$\Delta\left(\frac{1}{2Q}\right) = \frac{1}{2}\frac{f_{ut}}{f_{uts}}\left(\frac{1}{Q_{uts}} - \frac{1}{Q_{ut}} - \frac{1}{Q_{u0}}\frac{f_{uts}^2 - f_{ut}^2}{f_{u0}^2}\right); \tag{5}$$

where f_{uts} and Q_{uts} are the measured resonance frequency and Q-factor of the cavity with the quartz reactor containing the sample, respectively; f_{ut} and Q_{ut}, the homologous variables for no sample; and f_{u0} and Q_{u0}, without the quartz reactor (empty cavity). The conductivity is then calculated by

$$\sigma_{AC} = \omega\varepsilon_0 \frac{\eta\,\Delta\left(\frac{1}{2Q}\right)}{\left(\eta + N\frac{\Delta f}{f}\right)^2 + N^2\left[\Delta\left(\frac{1}{2Q}\right)\right]^2}, \tag{6}$$

with $N \in [0,1]$ representing the sample depolarization factor in the direction of the electric field polarization and η being the sample filling factor that quantifies the electric relative volume sample/cavity[10]. The parameters η and N depend on the specific geometry of the cavity, resonant mode (TM_{010}) and sample. They were determined through a calibration by measuring reference materials with known permittivity ($\eta = 0.00238$, $N = 0.102$)[1].

An example of application of this method is illustrated in the following graphs. Supplementary Figure 16 represents the reflection factor (S_{11}) of the microwave cavity (TM_{010} measurement mode) for a sample of porcelain (15 mm height, 10 mm diameter) in the quartz reactor measured at different temperatures when heated by microwaves. All the responses display the resonant peak of the cavity for each respective temperature and thereby include the information to determine their resonant frequencies and quality factors required in Eqs. (4) and (5) for dielectric or conductivity calculations according to the MCPT. The figure also shows the measurement of the empty cavity and the cavity with the quartz reactor tube without sample, also needed in the method.

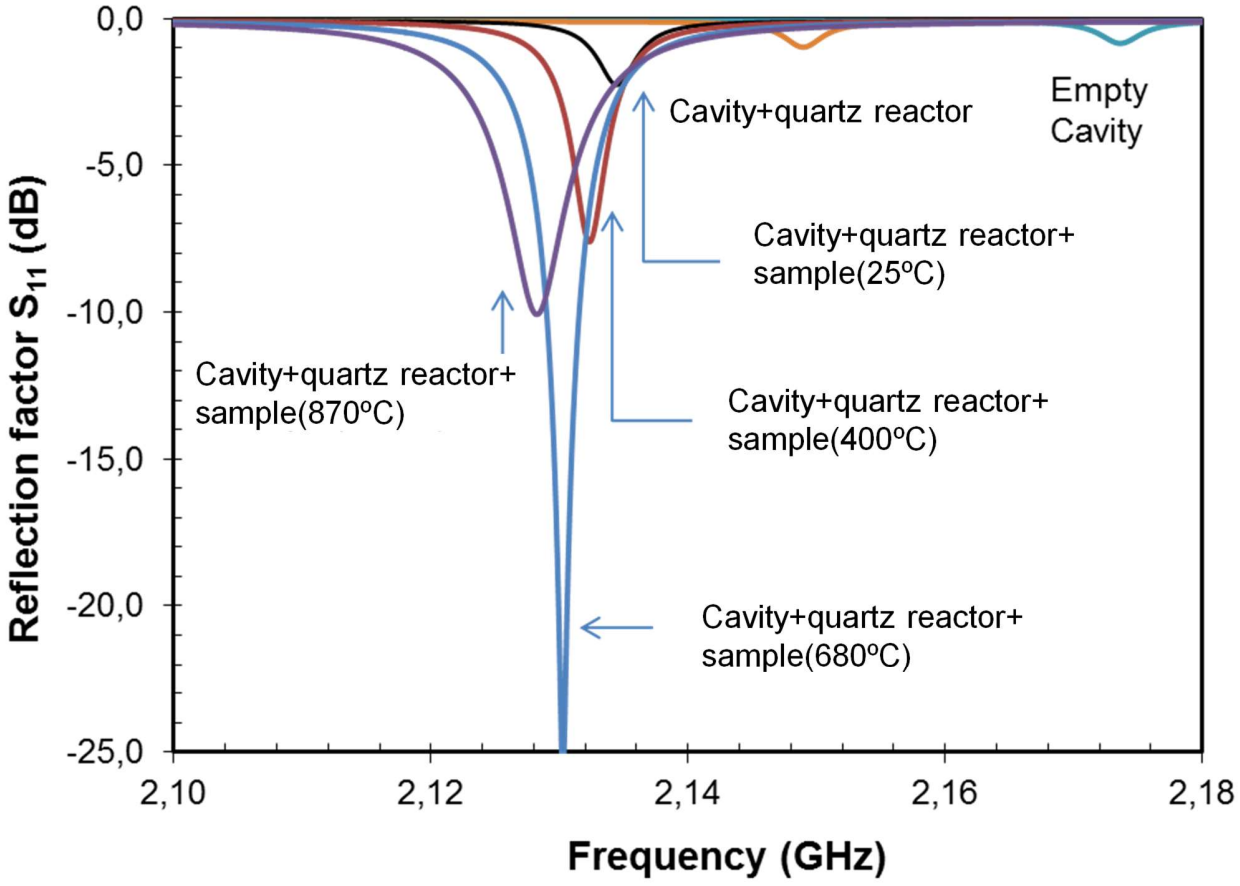

Supplementary Figure 16. Reflection factor of the microwave cavity (TM_{010} measurement mode) for a porcelain sample (15 mm height, 10 mm diameter) in the quartz reactor measured at different temperatures.

Therefore, the dynamic changes in the resonant frequency and Q-factor, derived from the measured reflection factor from the bottom of the cavity, were employed to calculate the conductivity of materials as a function of the temperature during microwave heating, according the MCPT described above. Supplementary Figure 17 displays the conductivity of the porcelain sample, calculated from Eq. (6), as a function of the temperature. The figure also plots the conductivity of the same sample heated by conventional means (see Supplementary Note 3 for conventional heating) for comparison purposes. In this representation, both conductivities overlap independently of the heating method employed.

The same procedure was applied to measure the a.c. conductivity of a sample of CGO in a redox process. Supplementary Figure 18 shows the Arrhenius plot of the conductivity during microwave and conventional heating of the sample. The conductivity upon conventional heating of the CGO sample follows an Arrhenius behavior characteristic of prevailing oxide-ion conduction. However, microwave heating emerges a distinct pattern and displays an abrupt increase in the conductivity profile upon reaching the induction temperature, T_{ind}, simultaneous to the material reduction,

provided the supplied microwave power exceeds a characteristic power threshold, P_{th}. Above 750 ºC both responses (microwave and conventional heating) seem to converge to the same values.

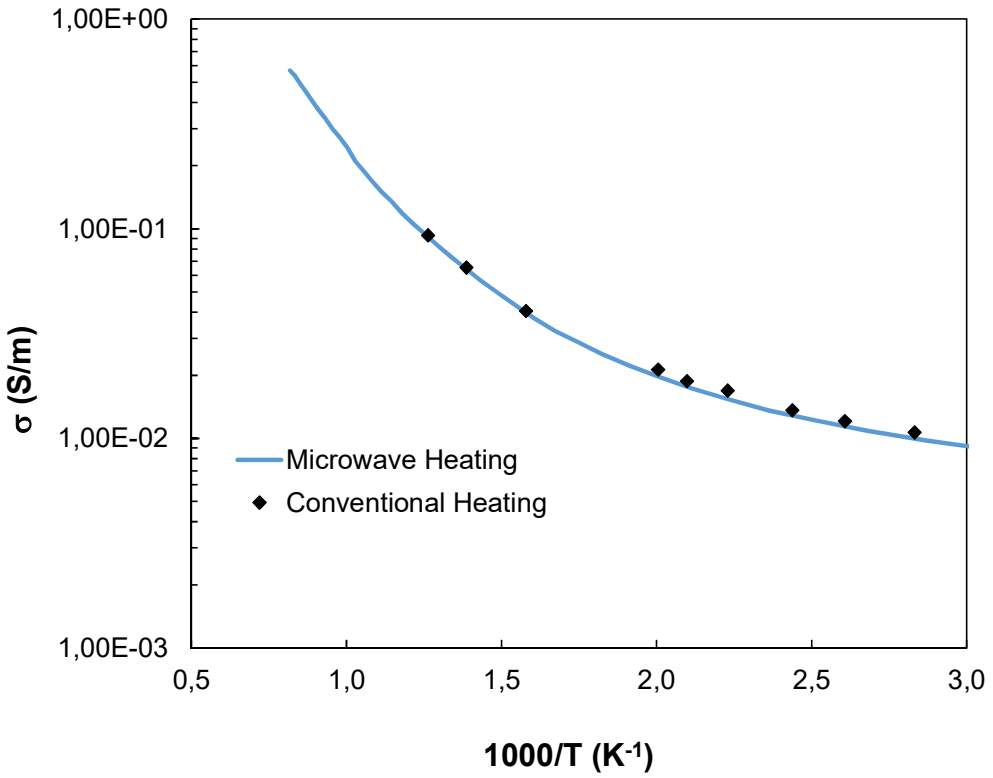

Supplementary Figure 17. Arrhenius plot of conductivity of a porcelain sample during microwave and conventional heating.

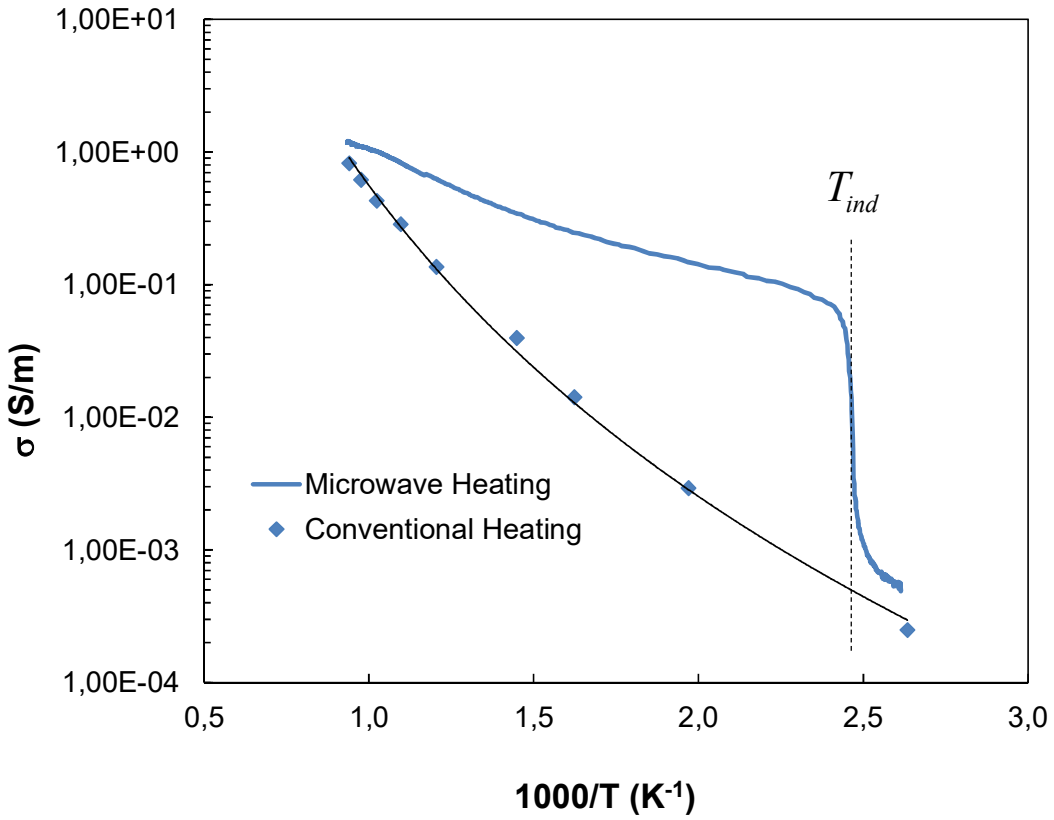

Supplementary Figure 18. Arrhenius plot of a.c. electric conductivity of a CGO sample during microwave and conventional heating.

The material capability to absorb energy from microwave radiation relies on both the peak frequency of the cavity and the material Q-factor, being these properties ultimately temperature dependent. In the low-temperature regime ($T < T_{ind}$), the material is unable to absorb large amounts of energy from the supplied power and only a low-to-moderate heating rate is possible. For temperatures above T_{ind}, however, the material can absorb much more energy from the cavity and has access to a broader range of radiation energies to take in, becoming very sensitive to the experiment conditions at the same time. The induction temperature is thus defined as the minimum temperature that enables the material to absorb enough microwave energy to promote its reduction. The induction temperature of a redox activated material is computed from the analysis of the Arrhenius plot of conductivity as a function of temperature.

The typical pattern of microwave heating is however not observed if the supplied microwave power is set below a given material-dependent power threshold, P_{th}. Fig. 2c (main text) displays very dissimilar conductivity patterns relying on the supplied power to be set above or below this power threshold. While the former case portraits the abrupt conductivity step rise and the material reduction, the latter appears to be alike to conventional heating. Indeed, these distinct scenarios

manifest that the material reduction is only triggered if enough microwave energy is supplied, even though the material has already reached the induction temperature.
In order to test the material power threshold, an initially hot CGO sample is, first, cooled down to 200 ºC in an oxidizing atmosphere (air) and, next, heated up with different microwave irradiation until thermal equilibrium is reached (Supplementary Figure 2). The supplied power is administered so that the absorbed energy is constant for each process. On the one hand, microwave-induced reduction is only observed for $P > P_{th}$ ~10 Wg^{-1}, unfolding a rapid immediate temperature rise followed by an asymptotical heating up to reach an equilibrium temperature, T_{eq}, the higher the more power is delivered to the samples. On the other hand, irradiated samples with $P < P_{th}$ yield a much smoother temperature time-evolution pattern once the microwaves are switched on, either a damped cooling down for lower microwave irradiation or a continuous moderate temperature rise for powers just below the threshold. Considering the latter scenario, the fact that a minimal increment on the sample absorbed energy implies a sizeable sharp temperature rise and a different heating pattern is just another manifestation that the present phenomena cannot be merely ascribed to a thermal effect. These very contrasting heating behavior, together with a notorious conductivity enhancement and the triggered oxygen release, evidence the reactive nature of the microwave-induced redox process.

Supplementary Note 6: Characterization of the electronic component of conductivity during microwave heating

The electrical conductivity, σ, of doped ceria is generally accepted as the sum of its electronic conductivity and ionic (oxygen vacancy) conductivity,

$$\sigma = \sigma_i + \sigma_e\,, \tag{7}$$

where each contribution is defined as the product of the mobility, μ, the electrical charge, Z, and the number of carriers, n, of that species:

$$\sigma_j = \mu_j Z_j n_j\,, \qquad j = i, e\,. \tag{8}$$

The electrical conductivity in doped ceria is an activated process and, therefore, sensitive to those parameters that modify the population of carriers or promote the mobility of any of the electrical carrier species. These are, for instance, temperature, oxygen partial pressure, dopant concentration or an external electric field. Typically, fluorite oxides, e.g. gadolinium-doped ceria $Ce_{1-y}Gd_yO_{2-y/2}$ (GDO), present an electrical conduction behavior of the type

$$\sigma_j T = A_j \exp\left(-E_{a,j}/k_B T\right), \qquad j = i, e\,; \tag{9}$$

for each carrier contribution, where E_a is the activation energy, A_j a temperature-independent parameter and k_B the Boltzmann constant.
The electronic conductivity component is obtained from data by subtracting of the ionic contribution to the overall conductivity measured for CGO during the material heating, attending to

Eq. (7). The measurement is performed in a reducing environment and no re-oxidation occurs during the material cooling down. This means that the population of carriers for the ionic and electronic species are only thermally activated after microwave-induced reduction. Considering that the ionic mobility is barely affected by the presence of the applied electric fields, it can be assumed that the ionic component to the conductivity is the same during the material heating up and cooling down, in other words, it is only temperature-dependent. In addition, the electronic mobility is no longer activated in absence of external electric fields and is negligible for the considered range of temperatures with respect to the ionic contribution. Hence, the ionic contribution during the microwave-induced heating can be approximated by the overall conductivity during the material cooling down.
Raw data is given in pairs of conductivity values, in $S \cdot m^{-1}$, and inverse temperature, 1000/T, in K^{-1}. The ionic component to be subtracted is calculated by linear interpolation of the conductivity values during the material cooling down at the temperatures of each measured data during heating up. The resulting electronic conductivity values during CGO microwave-assisted heating are represented in an Arrhenius plot, together with the measured data (Supplementary Figure 4). The electronic component is linearly fitted to the logarithmic representation of Eq. (9), i.e.

$$\log(\sigma_e T) = \log A_e - \frac{E_{a,e}}{k_B T} . \tag{10}$$

The obtained values for the activation energy for the electronic mobility and the pre-exponential factor are $E_{a,e}$ = 0.19 eV and A_e= $5.40 \cdot 10^3$ $S \cdot K \cdot m^{-1}$, respectively. Least-squares variance correlation for the linear fit yields r^2 = 0.994.

Supplementary Note 7: Impedance analysis in a resonant cavity

At high frequencies (>MHz), the intrinsic impedance of a medium is defined as the proportional relation between electric and magnetic fields of waves that propagate through the medium. This contrasts with the proportionality relation between voltage and current amplitudes in transmission lines or media restricted to low frequencies (~kHz). However, there is a complete duality between voltage-current solutions at lower frequencies and the wave solutions for the electric and magnetic fields at higher frequencies.
The intrinsic impedance of a medium, equal to the impedance of an electromagnetic wave that propagates through this medium, is expressed as the ratio of the transverse components of the electric and magnetic fields, also in units of ohms (Ω). For a transverse-electric-magnetic (TEM) plane and a homogeneous medium, the wave impedance is given by

$$Z = \frac{E_0^-(x)}{H_0^-(x)} \tag{11}$$

where $E_0^-(x)$ is the electric field and $H_0^-(x)$ is the magnetic field in phasor form. From this, it can be derived that

$$Z = \sqrt{\frac{\mu}{\varepsilon}} \tag{12}$$

with μ the medium magnetic permeability and ε the complex permittivity. If the medium has negligible magnetic properties, the impedance can be expressed as

$$Z = \sqrt{\frac{\mu}{\varepsilon}} = \sqrt{\frac{\mu_0}{\varepsilon_r \varepsilon_0}} = \frac{Z_0}{\sqrt{\varepsilon_r}} = \frac{Z_0}{\sqrt{(\varepsilon_r' - j\varepsilon_r'')}} \quad (13)$$

being Z_0 the impedance of free space (Z_0=120π Ω), ε_r' the medium relative dielectric constant and ε_r'' the relative loss factor. Then, the impedance can be determined directly from the dielectric properties of the medium

The described experimental procedure enables the simultaneous and contactless measurement of the a.c. conductivity and dielectric properties, together with the microwave heating of the sample. This allowed to measure the conductivity and dielectric properties variations in the same frequency range (GHz) as the frequency of the irradiation (~2.45 GHz) in order to have a better understanding of the polarization mechanism that dominates at these frequencies. However, a restriction of this experimental procedure is that conductivity measurements in the cavity reactor are only provided at single frequencies (the resonant frequencies of the cavity reactor) since the reactor is designed as a resonant cavity with two microwave operation modes (one for heating and another for measuring). Consequently, the impedance of the medium can only be provided at the resonant mode of the cavity reactor and evaluated as a function of the temperature during microwave heating, but not in broadband frequency range.

The following figure represents the real part of the impedance of the material, calculated from Eq. (13) in the microwave cavity during microwave heating. As a matter of fact, the induction temperature is also visible with this representation (Supplementary Figure 19).

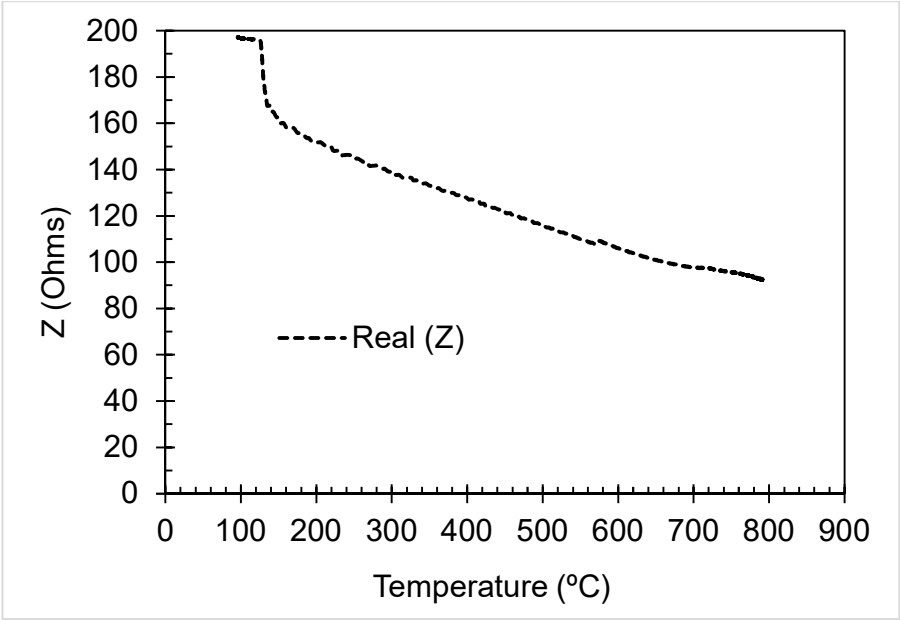

Supplementary Figure 19. Impedance (real part) of the CGO sample evaluated at the resonant frequency of the cavity as a function of temperature during microwave heating.

Supplementary Note 8: Electric field effect on conductivity

The presence of electric fields in ionic and polar materials notably modifies their conduction properties, being able to alter both the population of charge carriers and their mobility. Particularly, electric fields alter the transport activation energies of the charge carriers, their mobility being markedly sensitive to this effect. The activation energy for oxygen vacancy transport in thin-film SiO_2 dielectrics was firstly found to decrease for electric fields from up 10^6-10^7 V·cm^{-1}. The reported breakdown was linear with the applied field, F, (i.e., $\Delta E_a^F \propto -F$) within this range[11]. The effect was ascribed to the reduction of the energy barrier for oxygen vacancy diffusion. First principles calculations showed that this effect is common for oxygen vacancy and ion migration in metal oxides[12]. Nevertheless, the effect of an external electric field on polarons –the electronic carriers along with the perturbations caused on the surrounding lattice sites– is further significative. Its impact has been reported even for very low fields (e.g., $\sim 10^3$ V·cm^{-1} E-fields induced a percent level shift on the activation energy for the polaron hopping mobility in doped manganite strip films[13]). The localized polaron (or small polaron) configuration, however, breaks down in the presence of large E-fields since the polaron drifts amidst the atomic sites' neighborhood faster than it is required to cause localization; hence, polarons move through a delocalized band[14]. In the following, small polaron transport in the presence of a low-to-moderate electric field is considered.

Polaron hopping is a thermally activated migration process that originates from initial and final polaronic configurations matching an energy coincidence state[15]. This means that either the thermal or any externally driven vibrations must provide to the system enough energy to activate the polaron mobility. Furthermore, small polaron transport in transition metal oxides presents an adiabatic behavior [15]. That is, the hop probability to occur once a coincidence state is reached is the unity,

caused by a small lattice relaxation, t, during the inter-site transition. Considering a pair of equivalent lattice sites, the adiabatic polaron hopping rate can be derived from previous works[16,17]:

$$R_{\mathrm{ad}} = \nu \exp\left(\frac{E_a}{t}\right) \exp\left(\frac{-E_a}{k_B T}\right), \tag{14}$$

where ν is a representative atomic vibration mode and the first exponential term is related to the amount of vibrational free energy absorbed by the polaron during the hopping. The above equation manifests the empirically observed Meyer-Neldel compensation effect for polaron mobility. A reduction of the hopping activation energy leads to a greater polaron thermal activation for a given temperature T which also causes a decrease of the neat free vibrational energy of the lattice and thus a reduction of the entropy[16].

In absence of external electric fields, the hopping activation energy between equivalent lattice sites can be expressed as a sum contribution of short- and large-range electron-phonon interaction terms, respectively proportional to V_S and V_L, the short- and large-range electron-phonon interaction potentials

$$E_a(S) \approx \frac{V_S}{2R^3} + \frac{V_L}{2R}\left(\frac{1}{R} - \frac{1}{\sqrt{R^2 + S^2}}\right), \tag{15}$$

being the latter dependent on the polaron jump distance, S, and with R the localized states radii. Given that the required energy grows for long-distance migrations, small hops are favored. When an electric field, F, is applied in the direction of the hop, the activation energy lowers, yielding

$$E_a^F(S) = \frac{(4E_a(S) - eFaS\cos\theta)^2}{16E_a(S)}, \tag{16}$$

where a represents the interatomic separation and θ is the relative angle of the electric with respect to the jump[16]. Equally, the field-induced energy decrease for larger S shifts the hopping activation energy minimum for larger polaron jumps and, therefore, enhances the contribution of long-range electron-phonon interactions attending to Eq. (15). Consequently, the action of electric fields on the polaron dynamics induces a double effect: a direct reduction of the hopping activation energy and an increased long-range phonon interaction that enhances polaron hopping. The re-expression of Eq. (16) as a Taylor expansion around the minimum energy jump distance, $S_0 = \sqrt{V_L/eFa\cos\theta}$, yields

$$E_a^F(S) \approx E_a^{S\to\infty} + \sqrt{V_L eFa\cos\theta}\left(1 + \frac{(S - S_0)^2}{2SS_0}\right), \tag{17}$$

where $E_a^{S\to\infty} \approx V_L/2R$ embraces all the F- and S-independent contributions to the activation energy[16,17]. Considering that S_0 generally tends to approach the system's typical polaron hop distance, all the jump contributions from the previous equation can be neglected provided $(S - S_0)^2 \ll 2S_0^2$. Therefore, the adiabatic polaron hopping rate within an external electric field reflects the so-called Poole-Frenkel behavior displaying an exponential dependence with $(F^{1/2})$ [18]. This characteristic electric field-driven pattern, commonly found in insulator materials, has been

reported in many crystal structures and in disordered media like amorphous polymers involving small polaron transport[19].
Considering Eqs. (14) and (17**¡Error! No se encuentra el origen de la referencia.**), the analyzed electric field-assisted effects on polaron hopping, and thus the polaron mobility ($\mu_n \propto R_{\mathrm{ad}}$), can be summarized in

$$R_{\mathrm{ad}} \approx \nu \exp\left(\frac{E_a^{S\to\infty} + \sqrt{V_L eFa\cos\theta}}{k_B}\left(\frac{1}{T} - \frac{1}{T_0}\right)\right), \tag{18}$$

with $T_0 \equiv t/k_B$.

Supplementary Note 9: Thermodynamics of the O_2 and H_2 production through microwave generated oxygen vacancies and energy efficiency evaluation

The complete loop of hydrogen generation due to microwave-induced oxygen vacancy generation presents the next reactions:

$$\frac{1}{\delta_r - \delta_0} MO_{x-\delta_0} \xrightarrow{MW} \frac{1}{\delta_r - \delta_0} MO_{x-\delta_r} + \frac{1}{2}O_2 \qquad (r_{O2}) \quad (19)$$

$$\frac{1}{\delta_r - \delta_{ox}} MO_{x-\delta_r} + H_2O \rightarrow \frac{1}{\delta_r - \delta_{ox}} MO_{x-\delta_{ox}} + H_2 \qquad (r_{H2}) \quad (20)$$

where $MO_{x-\delta_0}$ is the initial state of the material; $MO_{x-\delta_r}$, the reduced material; and $MO_{x-\delta_{ox}}$, the re-oxidized material with steam; with δ_0, δ_r and δ_{ox} being the oxygen vacancy fractions for the material in the initial, reduced and re-oxidized forms. Therefore, the complete process involves the water dissociation through two reactions: (i) microwave-assisted oxygen generation and the formation of oxygen vacancies in the lattice, and (ii) hydrogen generation by the oxidation of these oxygen vacancies with the oxygen from water.

The efficiency of the process is evaluated considering the energy stored in form of hydrogen. For this purpose, the energy demand of the process is compared with the high heating value (HHV) of hydrogen (283.6 kJ/mol). The energy demand in this process entails the microwave energy and the heat required in the plant. The energy and properties for the pure gases were obtained from bibliography database[20].

Supplementary Note 10: Spontaneous formation of hydrogen in the material re-oxidation step with steam

Re-oxidation and vacancy generation reactions are connected through the water dissociation reaction,

$$H_2O \rightarrow H_2 + \frac{1}{2}O_2\,, \qquad (r_{H2O}) \qquad (21)$$

yielding

$$r_{H2} = r_{H2O} - r_{O2}\,. \qquad (22)$$

The spontaneous generation of hydrogen (r_{H2}) is achieved when its Gibbs free energy is negative:

$$\Delta G_{r_{H2}} = \Delta G_{r_{H2O}} - \Delta G_{r_{O2}} < 0\,, \qquad (23)$$

with

$$\Delta G_{r_{H2O}} = \Delta \mathrm{H}_{\mathrm{r_{H2O}}} - T \cdot \Delta S_{r_{H2O}}\,, \qquad (24)$$

$$\Delta S_{r_{H2O}} = 0.5 \cdot \Delta S_{O2} + \Delta S_{H2} - \Delta S_{H2O}\,; \qquad (25)$$

where T is the temperature and ΔG, ΔH and ΔS are the Gibbs free energy, the enthalpy and the entropy, respectively.

The equilibrium of the re-oxidation reaction is considered. For this purpose, the reaction (r_{H2}) is conveniently re-expressed in terms of lattice terms,

$$2Ce'_{Ce} + V_O^{\cdot\cdot} + H_2O \rightleftarrows 2Ce_{Ce}^X + O_O^X + H_2\,, \qquad (r_{H2'}) \qquad (26)$$

where Ce'_{Ce} and Ce_{Ce}^X refer to cerium atoms in cerium lattice sites with a single electron excess and no excess, respectively; and O_O^X and $V_O^{\cdot\cdot}$ represent, correspondingly, oxygen and vacancies in oxygen sites. This description allows to evaluate the equilibrium of the reaction considering the equations (27-32).

Attending to the law of mass action, the Gibbs free energy is related to the reactant's concentrations through

$$K_{EQ,rH2'} \equiv \exp\left(-\frac{\Delta G_{rH2}}{RT}\right) = \frac{[O_O^X] \cdot [Ce_{Ce}^X]^2 \cdot pH2}{[V_O^{\cdot\cdot}] \cdot [Ce'_{Ce}]^2 \cdot pH2O}, \qquad (27)$$

with K_{EQ} defining the equilibrium constant of ($r_{H2'}$) and pH_2 and pH_2O, the partial pressures of hydrogen and steam, respectively. This equation simplifies considering that the concentration ratios of oxygen vacancies with respect to oxygen sites and reduced to non-reduced ceria can be re-expressed as in

$$\frac{[O_O^X]}{[V_O^{\cdot\cdot}]} = \frac{O - \delta_{ox}}{\delta_{ox}}, \qquad (28)$$

$$\frac{[Ce_{Ce}^X]}{[Ce'_{Ce}]} = \frac{1 - Xd - 2 \cdot \delta_{ox}}{2 \cdot \delta_{ox}}, \qquad (29)$$

where Xd is the fraction of dopant agent (0 for CeO_2 and CZO, and 0.2 for CGO) and O is the oxygen fraction in the lattice (2 for CeO_2 and CZO, and 1.9 for CGO). In addition, the partial pressures' ratio is

$$\frac{pH2}{pH2O} = \frac{X}{1 + a_{excess} - X}\,, \tag{30}$$

being a_{excess} the additional water fraction introduced above the stoichiometry and X, the oxygen vacancy conversion, which further relates the oxygen vacancy fractions for the reduced and re-oxidized forms through

$$\delta_{ox} = \delta_r \cdot (1 - X)\,. \tag{31}$$

Considering the oxidation analysis, the specific hydrogen that can be generated per mass of material (F_{H2}) within this loop process can be quantified considering the hydrogen and the material molar weights, respectively MW_{H2} and MW_{mat}, so that

$$F_{H2} = (\delta_r - \delta_{ox}) \cdot \frac{MW_{H2}}{MW_{mat}}\,. \tag{32}$$

The re-oxidation of the reduced material could not recover the initial state ($\delta_{ox} > \delta_0$). This means that some of the oxygen vacancies generated in the first reduction step will not be later re-oxidized with steam. However, subsequent reduction-oxidation cycles reach the same amount of oxygen vacancies (δ_r), and the generated hydrogen is proportional to the jump between the reduced and the oxidized states, ($\delta_r - \delta_{ox}$), (Supplementary Figure 20). Further calculations, e.g. the evaluation of the energy cost to generate hydrogen, were made under this consideration.

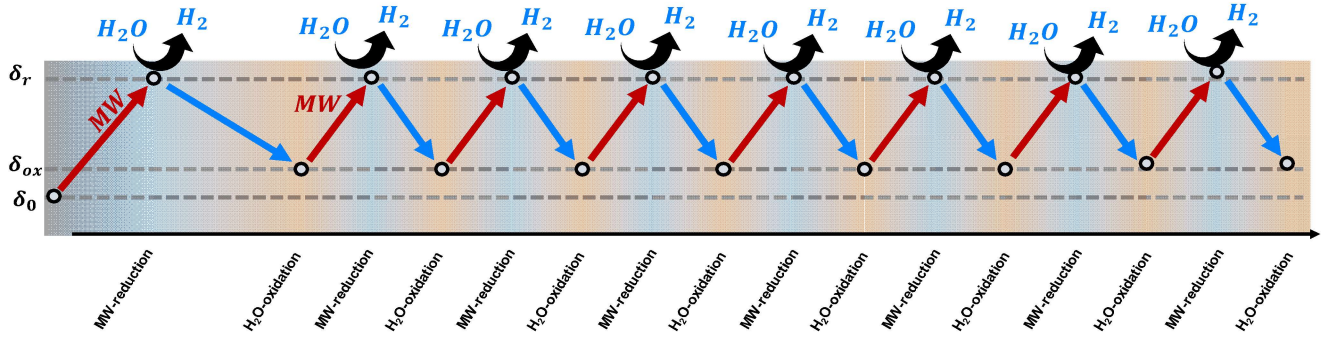

Supplementary Figure 20. Schematics of the sequential reduction-oxidation cycles.

Supplementary Note 11: Evaluation method for the energy cost of the hydrogen generated and efficiency of the process

1. Evaluation of the MW energy

Microwave generators are composed basically by a high-voltage power supply and a magnetron. The power supply provides a high-voltage DC current needed by the magnetron to generate the high-power microwave signal. Energy efficiency of the power supply can be as high as 95%, while magnetron efficiency is around 88-90%, so conversion from electricity to microwave energy has a global efficiency of >85%. The supplied microwave energy is mostly absorbed by the system either to promote the material's reduction (r_{O2}) or to be converted into heat (Fig. 2e in main text), with a non-absorbed energy yield (η_{MW}) sized around 5% and a efficiency of conversion from electricity to microwave energy (η_{ELEC}) of 85%. The fraction of energy involved in the reduction reaction with respect to the total absorbed energy is parametrized by f_r, while η_{MW} is fixed to 5% in the present study. The energy demand to form oxygen vacancies corresponds to the enthalpy of this reaction, provided it is an endothermic reaction. However, the entropic contribution requires to be satisfied by means of heat. These two contributions, namely the Gibbs free energy contribution (ΔG_{rO_2}), emerge as the necessary amount of energy to be covered in order to develop the reduction reaction. Taking the balance from the initial input microwave energy to the energy used in the reduction reaction, the overall microwave energy (P) can be expressed in terms of the previous parameters, η_{MW} and f_r, and the reaction enthalpy and entropy,

$$P = \frac{\Delta G_{rO_2}}{(1-\eta_{MW})\cdot \eta_{ELEC}\cdot f_r} = \frac{\Delta H_{r_{O2}} - T\cdot \Delta S_{r_{O2}}}{(1-\eta_{MW})\cdot \eta_{ELEC}\cdot f_r}. \quad (33)$$

2. Evaluation method for the heat demand of the process

This analysis was evaluated considering isothermal reduction and re-oxidation at 350 °C. The heat demand of the process mainly originates from the evaporation of water at room temperature up to the temperature of the process ($Heat_{H2O} = 57.64$ kJ/mol). Otherwise, different heat intakes can be recovered from the outlet streams: (i) the oxygen cooling down to until room temperature ($Heat_{O2} = 10.14$ kJ/mol), (ii) the cooling of the hydrogen-water mixture and (iii) the heat release in the re-oxidation (r_{H2}). Taking into account the difficulty to recover the condensation energy, the heat that can be recovered from the hydrogen-water hot stream ($Heat_{exhau}$) was evaluated for cooling down from the process temperature to 105 °C. This energy depends on the excess fraction of water introduced on the process (a_{excess}), i.e.

$$Heat_{exhaust} = Heat_{H2} + a_{excess}\cdot Heat_{STEAM}\,, \quad (34)$$

with $Heat_{H2} = 7.18$ kJ/mol and $Heat_{STEAM} = 8.68$ kJ/mol.

Finally, the Balance of Plant heat ($Heat_{BoP}$) is defined as the system neat heat required as input. That is, the difference between water heating demands and the recovered heat, considering the fraction of heat losses during the process, which are set to $\eta_{heat} = 5\%$ in this study. It reads

$$Heat_{BoP} = \frac{Heat_{H2O} \cdot (1 + a_{excess})}{1 - \eta_{heat}} - (1 - \eta_{heat}) \cdot \left(Heat_{exhaust} + \frac{Heat_{O2}}{2} \right) \quad (35)$$

3. Evaluation of the heat from Microwaves

Microwave irradiation of the material implies a fraction of the absorbed energy (1-f_r) to develop into heat, i.e.

$$P \cdot \eta_{ELEC} \cdot (1 - \eta_{MW}) \cdot (1 - f_r)\,, \quad (36)$$

with some of this energy evolving into the entropic contribution of the material reduction as a heat demand ($T \cdot \Delta S_{r_{O_2}}$). Additionally, the heat released during the re-oxidation emerges from the difference of enthalpies between the oxygen vacancy generation and the water dissociation,

$$\Delta H_{r_{O_2}} - \Delta H_{rH2O}\,. \quad (37)$$

Therefore, the heat balance of the microwave driven reduction ($Heat_{MW}$), obtained from the simultaneous oxygen vacancy generation and heat excess recovery from the re-oxidation step, yields

$$Heat_{MW} = (1 - \eta_{heat}) \cdot \left(P \cdot \eta_{ELEC} \cdot (1 - \eta_{MW}) \cdot (1 - f_r) + \left(\Delta H_{rO_2} - \Delta H_{rH2O} \right) \right) - T \cdot \Delta S_{r_{O_2}}\,. \quad (38)$$

Supplementary Note 12: Evaluation method for the efficiency and the energy cost of the hydrogen generation

The efficiency analysis in hydrogen generation process is evaluated considering the energy demand of the process regarding the High Heating Value (HHV). For hydrogen, the HHV is 283.6 kJ/mol. The energy demand was evaluated under two scenarios (Supplementary Table 1): (case i) considering only the electric demand of the process and (case ii) considering both the heat and the electric demands. Being the microwave heating inherent to the assisted reduction of the material, the entropic heat demand of this reaction is generally covered. Otherwise, an external heat intake must be supplied, i.e. in those cases where the neat heat of the microwave process requires external energy ($Heat_{MW} < 0$), as contemplated in the second term in Eq. (39).

Supplementary Table 1. Evaluation of the overall energy demand of the hydrogen generation.

Case	MW electric	BoP	Equation	Id
i	✓	×	$P_I = \frac{\Delta H_{rO2} - T \cdot \Delta S_{r_{O_2}}^{ref}}{\left(1 - \eta_{MW}\right) \cdot \eta_{ELEC} \cdot f_r} - min(0,\, Heat_{MW})$	(39)
ii	✓	✓	$P_{II} = P_I + Heat_{BoP}$	(40)

Therefore, the energy efficiency (eff) for the hydrogen generation process is evaluated depending on the case:

$$eff = \frac{HHV}{P_i}, \quad i = I, II. \tag{41}$$

Supplementary Table 2 shows the hydrogen energy cost data for other considered technologies.

Supplementary Table 2. Energy demand ranges considered for other hydrogen generation processes based on water dissociation.

Technology	Hydrogen energy cost (kWh/kg H_2)	Source
PEM electrolysis	52 – 65	21–25
Alkaline electrolysis	47 – 70	21,22,24–27
Solar thermochemical	> 65	24,28–38

In general, the processes operating at higher temperature show lower efficiencies since different mass streams should be heated and cooled down, which implies important increments in entropy, and results in inevitable heat dissipations. For the case of solar thermal processes and apart from radiative losses, the main losses are caused by heating/cooling of fluids and ceramics (oxygen/vacancy carriers) and in a minor extent to inert gas consumption, non-uniform temperature and fluid flow distribution in the solar reactor[24,28,31,33].

Supplementary Note 13: Thermodynamic data of the different compounds

The thermodynamic data for the different materials tested were compiled from bibliography.

Supplementary Table 3. Properties of the materials.

Material	ΔH_r (kJ/mol$_O$)	ΔS_r (J/mol$_O$/K)	Source
CGO	385	*	39,40
CeO_2	450	*	40,41
CZO	$-\frac{7148.8 \cdot \delta^2 - 2306.6 \cdot \delta - 568.67}{2}$	$-\frac{348.83 \cdot \delta - 345.07}{2}$	42,43

In Supplementary Figure 21, the expression for the entropy of CeO_2 depending on the oxygen vacancies was evaluated considering the results of previous authors[42]. For the CGO, the entropy was evaluated considering that the oxygen vacancy does not affect to the enthalpy and using the results reported by Gauckler et al.[44].

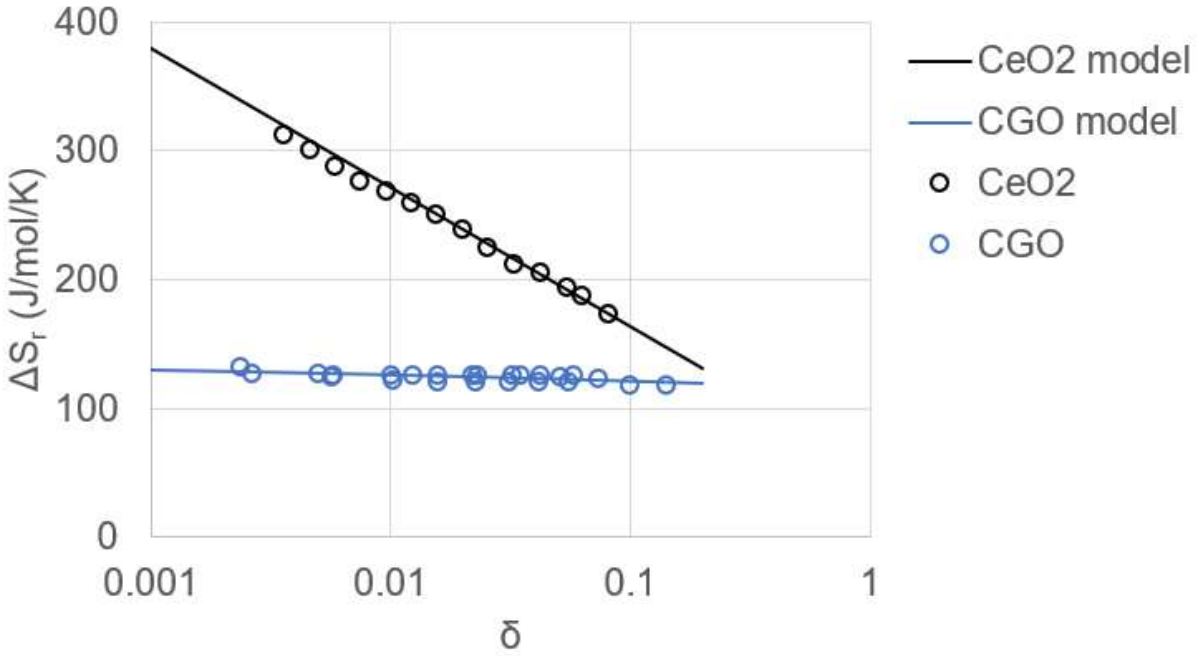

Supplementary Figure 21. Entropy associated to the reduction process of the material.

The evaluation of the thermodynamic variables ΔH_r, ΔS_r and $\Delta G_r \equiv \Delta H_r - T \cdot \Delta S_r$ in the reduction process was performed through integration along the intermediate states described in terms of δ, according to Supplementary Table 3. As an example, the Gibbs free energy between the initial oxidized state (δ_{ox}) until the final reduced state (δ_r) reads

$$\Delta G_r = \frac{1}{\delta_r - \delta_{ox}} \int_{\delta_{ox}}^{\delta_r} \Delta G_r(\delta) d\delta \tag{42}$$

Supplementary Note 14: Techno-economic estimation of the capital cost

The Capital Expenditure (CAPEX) was evaluated for hydrogen generation via water splitting triggered by the microwave-driven reduction of metallic oxides. A comparison was established for hydrogen generation systems based on different electrolysis technologies. A diagrammatic view of these two types of systems is depicted in Supplementary Figure 22, divided into the following blocks: (**A**) Heat management system; (**B**) specific block, i.e. electrolysis or MW system; (**C**) condensation and (**D**) compression system. The estimation of the non-specific blocks was calculated with the same engineering correlations.

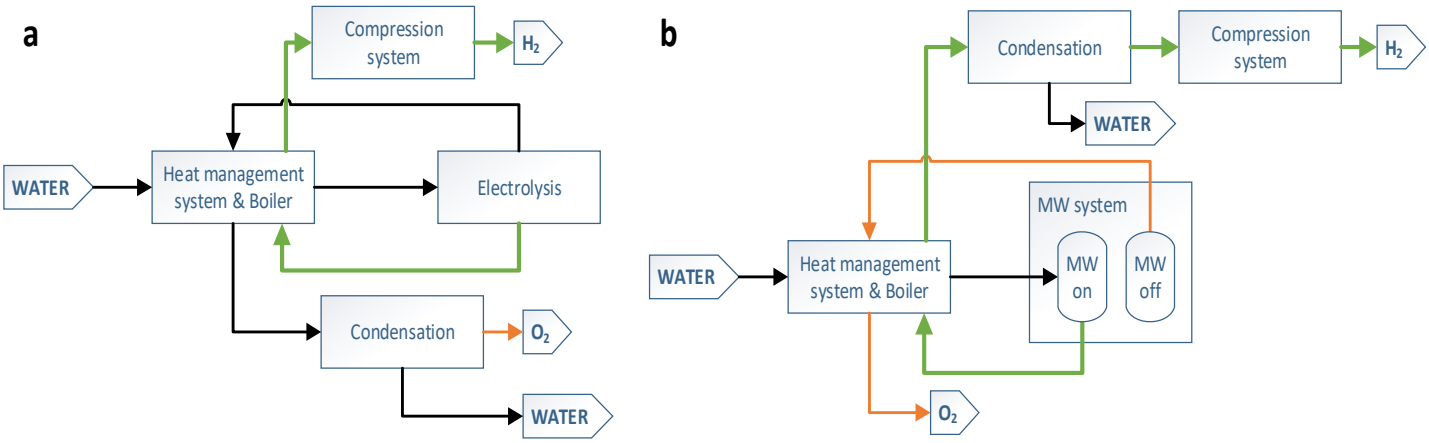

Supplementary Figure 22. Block diagrams of the H_2 generation system considering **a,** electrolysis and **b,** a MW assisted process.

The capital costs were calculated for two scales of H_2 generation plants: a distributed case (10 kg/day of hydrogen) and centralized case (50000 kg/day). Two different scenarios were additionally considered: current and future. The non-specific costs of the microwave system are collected in Supplementary Table 4 based on previous studies on electrolysis systems[45] (those items lacking future estimation in the bibliography were evaluated considering the 75% of their respective current costs). They are classified as uninstalled cost, representing the installation expenses; mechanical BoP cost, i.e. the price of the units of the plant (excluding the specific block units and additional process like compression blocks); and electrical BoP cost, the price of the rectifier and the a.c. transformer. Furthermore, an extra cost was incorporated adding up a 10% and 2.5% of the main unit and BoP costs for the distributed and centralized plants, respectively.

Supplementary Table 4. Cost of the microwave system (except for specific block). [a] represents a percentage from the unit costs (BoP).

	Units	Distributed plant		Centralized plant	
		Current	Future	Current	Future
Uninstalled cost	*$/kW*	599	379	460	233
Mechanical BoP cost	*$/kW*	136	140	36	23
Electrical BoP cost	*$/kW*	121	97	82	68
Other costs	*%*[a]	10	10	2.5	2.5

The cost of the specific block (**B**) of the microwave system was subdivided into two units: the reactor the microwave generation units, both computed from different engineering correlations [46–48] and own market analysis. The microwave generator costs are shown in Supplementary Table 5, while the process parameters for the microwave system were evaluated and upscaled attending to the values reflected in Supplementary Table 6. Once included the MW system costs, which gather around 55 – 70% of the overall capital costs, the breakdown of the CAPEX is reported in Supplementary Table 7.

Supplementary Table 5. Specific cost for the microwave generator.

	Units	Distributed plant		Centralized plant	
		Current	Future	Current	Future
Microwave generation*	*$/kW*	800 – 1200	600 – 900	400 – 700	300 – 525

Supplementary Table 6. Process parameters considered for plant dimensioning and cost evaluation of the MW system.

Parameter	Value	Units
Specific hydrogen per kg of material per cycle	0.2	*g H_2/kg* material
Density of the material	7.22	*g/cm^3*
Porosity of the solid in the bed	40	*%*
f_r	80	*%*
MW generation efficiency	90	*%*
Power demanded by distributed MW-based plant	21.22	*kW*
Power demanded by centralized MW-based plant	106.11	*MW*

The specific hydrogen generated per mass of material determines the size of the reactor unit and, consequently, it is a critical factor considering the capital cost analysis. Supplementary Figure 23 shows the evolution of the capital cost of the distributed plant (10 kg of H_2 per day).

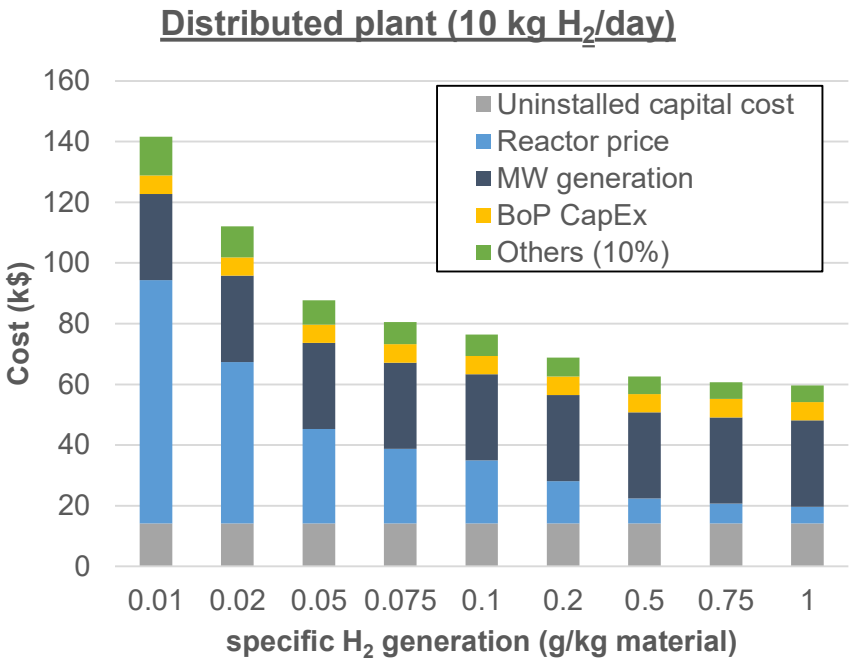

Supplementary Figure 23. Evolution of the capital cost depending on the specific H2 generated per mass of material.

Supplementary Table 7. Evaluation of the CAPEX for the MW-based generation of H_2. k$: 1000$; M$: 10^6 $. [a]: 1200 $/kW; [b]: 900 $/kW; [c]: 700 $/kW; [d]: 525 $/kW; [e]: other cost was estimated considering an additional cost of 10% for the distributed plant and 2.5% for the centralized plant.

	Distributed (10 *kg/day*)			**Centralized (50000 *kg/day*)**		
	Current	**Future**	**Units**	**Current**	**Future**	**Units**
Uninstalled cost	**14.17**	**8.96**	*k$*	**54.40**	**27.55**	*M$*
MW system						
Reactor unit	13.91	10.43	*k$*	2.51	*1.83*	*M$*
MW generation	28.38[a]	21.29[b]	*k$*	82.78[c]	62.09[d]	*M$*
Subtotal MW system	**42.29**	**31.72**	*k$*	**85.29**	**63.92**	*M$*
BoP						
Mechanical BoP	3.22	3.31	*k$*	4.26	2.72	*M$*
Electrical BoP	2.86	2.29	*k$*	9.70	8.04	*M$*
Subtotal BoP	**6.08**	**5.61**	*k$*	**13.95**	**10.76**	*M$*
Other[e]	**4.84**	**3.73**	*k$*	**2.48**	**1.87**	*M$*
CAPEX	**67.37**	**50.02**	*k$*	**156.13**	**104.10**	*M$*

The CAPEX comparison of the microwave technology with respect to different electrolysis technologies was evaluated for the distributed and centralized cases, in current and future scenarios. The energy demand of these plants was evaluated considering 57.9 kWh/kg of H_2 and 68% of overall efficiency. This leads to an energy demand of 35.48 kW for the distributed plant (10 kg/day) and 177.39 MW for the centralized plant (50000 kg/day).

Different correlations have been obtained from bibliography. Peterson et al.[45] evaluated the CAPEX of the PEM electrolysis, divided into four items: (i) uninstalled capital costs, (ii) Stack capital cost; (iii) Mechanical BoP (consisting the water pumping, heat exchanging management, condenser and other equipment) and (iv) electrical BoP (AC to DC rectifier and AC transformer). Matute et al. [49] estimated the CAPEX for alkaline and PEM attending to previous reports[50–52]. CAPEX in these works includes stack, balance of plant, and power supply. Ulleberg et al.[53] made an estimation for alkaline electrolyser in small scale plants including the electrolysis system, the pressurization and the installation cost and Ferrero et al.[54] made a comparison of PEM, alkaline and SOEC electrolysis systems based on previous works[52,55,56]. A general display of the H_2 generation processes based on microwaves and electrolysis is shown in Supplementary Table 8.

Supplementary Table 8. CAPEX comparison of the MW and electrolysis hydrogen generation processes considering different technologies.

	Distributed (10 *kg/day*)			**Centralized (50000 *kg/day*)**			
	Current	**Future**	**Units**	**Current**	**Future**	**Units**	**Source**
MW	*57 - 67*	*42 - 50*	*k$*	120 - 156	77 - 105	*M$*	
PEM	40 - 80	*10 - 40*	*k$*	160 - 400	*40 - 180*	*M$*	[49–52,54,57]
Alkaline	35 - 100	13 - 65	*k$*	170 - 530	65-165	*M$*	[49–54]
SOC	213	17.7	*k$*	1065	88.7	*M$*	[54]

Supplementary References

1. Catalá-Civera, J. M. *et al.* Dynamic Measurement of Dielectric Properties of Materials at High Temperature During Microwave Heating in a Dual Mode Cylindrical Cavity. *IEEE Trans. Microw. Theory Tech.* **63**, 2905–2914.

2. Balanis, C. A. *Advanced Engineering Electromagnetics*. (John Wiley and Sons, 1989).

3. Arai, M., Binner, J. G. P. & Cross, T. E. Comparison of Techniques for Measuring High-Temperature Microwave Complex Permittivity: Measurements on an Alumina/Zircona System. *J. Microw. Power Electromagn. Energy* **31**, 12–18 (1996).

4. Krupka, J. Contactless methods of conductivity and sheet resistance measurement for semiconductors, conductors and superconductors. *Meas. Sci. Technol.* **24**, 62001 (2013).

5. Hsieh, H., Goldey, J. M. & Brown, S. C. A Resonant Cavity Study of Semiconductors. *J. Appl. Phys.* **25**, 302–307 (1954).

6. Warman, J. M., Gelinck, G. H. & Haas, M. P. de. The mobility and relaxation kinetics of charge carriers in molecular materials studied by means of pulse-radiolysis time-resolved microwave conductivity: dialkoxy-substituted phenylene-vinylene polymers. *J. Phys. Condens. Matter* **14**, 9935–9954 (2002).

7. Park, J., Reid, O. G., Blackburn, J. L. & Rumbles, G. Photoinduced spontaneous free-carrier generation in semiconducting single-walled carbon nanotubes. *Nat. Commun.* **6**, 8809 (2015).

8. Honsho, Y., Miyakai, T., Sakurai, T., Saeki, A. & Seki, S. Evaluation of Intrinsic Charge Carrier Transport at Insulator-Semiconductor Interfaces Probed by a Non-Contact Microwave-Based Technique. *Sci. Rep.* **3**, 3182 (2013).

9. Eichelbaum, M. *et al.* The microwave cavity perturbation technique for contact-free and in situ electrical conductivity measurements in catalysis and materials science. *Phys. Chem. Chem. Phys.* **14**, 1302–1312 (2012).

10. Altschuler, H. M. *Handbook of Microwave Measurements*. vol. 2 (USA: Polytech. Inst. Brooklyn Press, 1963).

11. McPherson, J. W. & Mogul, H. C. Underlying physics of the thermochemical e model in describing low-field time-dependent dielectric breakdown in SiO2 thin films. *J. Appl. Phys.* **84**, 1513–1523 (1998).

12. El-Sayed, A. M., Watkins, M. B., Grasser, T. & Shluger, A. L. Effect of electric field on migration of defects in oxides: Vacancies and interstitials in bulk MgO. *Phys. Rev. B* **98**, 064102 (2018).

13. Kuang, H. *et al.* Electric field control of the small-polaron hopping conduction in spatial confined Pr0.7(Ca0.6Sr0.4)0.3MnO3/PMN-PT heterostructure. *AIP Adv.* **7**, 055814 (2017).

14. Hed, A. Z. & Freud, P. J. Instability of the localized small polaron in high electric fields. *J. Non. Cryst. Solids* **2**, 484–495 (1970).

15. Holstein, T. Studies of polaron motion. Part II. The 'small' polaron. *Ann. Phys. (N. Y).* **8**, 343–389 (1959).

16. Emin, D. Generalized adiabatic polaron hopping: Meyer-neldel compensation and poole-frenkel behavior. *Phys. Rev. Lett.* **100**, 166602 (2008).

17. Emin, D. Formation and hopping motion of molecular polarons. *Phys. Rev. B - Condens. Matter Mater. Phys.* **61**, 14543–14553 (2000).

18. Frenkel, J. On pre-breakdown phenomena in insulators and electronic semi-conductors [3]. *Physical Review* vol. 54 647–648 (1938).

19. Borsenberger, P. M. & Schein, L. B. Hole transport in 1-phenyl-3-((diethylamino)styryl)-5-(p-(diethylamino) phenyl)pyrazoline-doped polymers. *J. Phys. Chem.* **98**, 233–239 (1994).

20. Bruce E. Poling John O' Connell, J. M. P. *The properties of gases and liquids. 5th edition.* (McGraw-Hill Education, 2000).

21. (IRENA), I. R. E. A. & Gielen, D. *Hydrogen from renewable power: Technology outlook for the energy transition*. https://www.irena.org/-/media/Files/IRENA/Agency/Publication/2018/Sep/IRENA_Hydrogen_from_renewable_power_2018.pdf (2018).

22. Posdziech, O., Schwarze, K. & Brabandt, J. Efficient hydrogen production for industry and electricity storage via high-temperature electrolysis. *Int. J. Hydrogen Energy* **44**, 19089–19101 (2019).

23. Maric, R. & Yu, H. Proton exchange membrane water electrolysis as a promising technology for hydrogen production and energy storage. in *Nanostructures in Energy Generation, Transmission and Storage* (IntechOpen, 2018).

24. Dincer, I. & Acar, C. Review and evaluation of hydrogen production methods for better sustainability. *Int. J. Hydrogen Energy* **40**, 11094–11111 (2015).

25. Kuckshinrichs, W., Ketelaer, T. & Koj, J. C. Economic analysis of improved alkaline water electrolysis. *Front. Energy Res.* **5**, 1 (2017).

26. Holladay, J. D., Hu, J., King, D. L. & Wang, Y. An overview of hydrogen production technologies. *Catalysis Today* vol. 139 244–260 (2009).

27. Perret, R. *Solar Thermochemical Hydrogen Production Research (STCH)*. http://www.osti.gov/servlets/purl/1219357/ (2011) doi:10.2172/1219357.

28. Moser, M., Pecchi, M. & Fend, T. Techno-economic assessment of solar hydrogen production by means of thermo-chemical cycles. *Energies* **12**, 352 (2019).

29. Marxer, D., Furler, P., Takacs, M. & Steinfeld, A. Solar thermochemical splitting of CO2 into separate streams of CO and O2 with high selectivity, stability, conversion, and efficiency. *Energy Environ. Sci.* **10**, 1142–1149 (2017).

30. Bishop, S. R., Duncan, K. L. & Wachsman, E. D. Surface and bulk oxygen non-stoichiometry and bulk chemical expansion in gadolinium-doped cerium oxide. *Acta Mater.* **57**, 3596–3605 (2009).

31. Suzuki, T., Kosacki, I. & Anderson, H. U. Defect and Mixed Conductivity in Nanocrystalline Doped Cerium Oxide. *J. Am. Ceram. Soc.* **85**, 1492–1498 (2002).

32. Gopal, C. B. & van de Walle, A. Ab initio thermodynamics of intrinsic oxygen vacancies in ceria. *Phys. Rev. B* **86**, 134117 (2012).

33. Takacs, M., Scheffe, J. R. & Steinfeld, A. Oxygen nonstoichiometry and thermodynamic characterization of Zr doped ceria in the 1573–1773 K temperature range. *Phys. Chem. Chem. Phys.* **17**, 7813–7822 (2015).

34. Ganzoury, M. A., Fateen, S.-E. K., El Sheltawy, S. T., Radwan, A. M. & Allam, N. K. Thermodynamic and efficiency analysis of solar thermochemical water splitting using Ce–Zr mixtures. *Sol. Energy* **135**, 154–162 (2016).

35. Gauckler, L. J., Go¨dickemeier, M. & Schneider, D. Nonstoichiometry and Defect Chemistry of Ceria Solid Solutions. *J. Electroceramics* **1**, 165–172 (1997).

36. Peterson, D. *et al. DOE Hydrogen and Fuel Cells Program Record Title: Hydrogen Production Cost From PEM Electrolysis-2019*. http://www.hydrogen.energy.gov/h2a_prod_studies.html: (2019).

37. Lovegrove, K. *et al. Renewable energy options for industrial process heat. Appendix E*. (2019).

38. Woods, D. R. Appendix D: Capital Cost Guidelines. in *Rules of Thumb in Engineering Practice* 376–436 (Wiley-VCH Verlag GmbH & Co. KGaA, 2007). doi:10.1002/9783527611119.app4.

39. *ChE 456 Spring 2002 Major 2 Ethylene Oxide Production*.

40. Matute, G., Yusta, J. M. & Correas, L. C. Techno-economic modelling of water electrolysers in the range of several MW to provide grid services while generating hydrogen for different applications: A case study in Spain applied to mobility with FCEVs. *Int. J. Hydrogen Energy* **44**, 17431–17442 (2019).

41. Bertuccioli, L. *et al.* Development of water electrolysis in the European Union.

42. E, T. & Engie, H. *Study on early business cases for H2 in energy storage and more broadly power to H2 applications*. https://www.fch.europa.eu/sites/default/files/P2H_Full_Study_FCHJU.pdf (2017).

43. *Fuel Cells and Hydrogen Joint Undertaking (FCH JU) Multi-Annual Work Program 2014-2020*.

44. Ulleberg, Ø. & Hancke, R. Techno-economic calculations of small-scale hydrogen supply systems for zero emission transport in Norway. *Int. J. Hydrogen Energy* **45**, 1201–1211 (2020).

45. Ferrero, D., Gamba, M., Lanzini, A. & Santarelli, M. Power-to-Gas Hydrogen: Techno-economic Assessment of Processes towards a Multi-purpose Energy Carrier. in *Energy Procedia* vol. 101 50–57 (Elsevier Ltd, 2016).

46. Commercialisation of Energy Storage. (2015).

47. Schiller, H. Demonstration of 500kWe alkaline fuel cell system with heat capture. http://www.fch.europa.eu/sites/default/files/5-POWER-UP_update151111 (ID 2848023) (ID 2848602).pdf. (2016).

48. Peterson, D., Vickers, J. & DeSantis, D. *Hydrogen Production CostFrom PEM Electrolysis-2019*. (2020).

49. Emamdoust, A. *et al.* Partial oxidation of methane over SiO2 supported Ni and NiCe catalysts. *J. Energy Chem.* **47**, 1–9 (2020).

50. Osman, A. I. Catalytic Hydrogen Production from Methane Partial Oxidation: Mechanism and Kinetic Study. *Chem. Eng. Technol.* **43**, 641–648 (2020).

51. Sengodan, S. *et al.* Advances in reforming and partial oxidation of hydrocarbons for hydrogen production and fuel cell applications. *Renew. Sustain. Energy Rev.* **82**, 761–780 (2018).

52. Otsuka, K., Wang, Y., Sunada, E. & Yamanaka, I. Direct Partial Oxidation of Methane to Synthesis Gas by Cerium Oxide. *J. Catal.* **175**, 152–160 (1998).

53. Kikuchi, E. & Chen, Y. Syngas Formation by Partial Oxidation of Methane in Palladium Membrane Reactor. *Stud. Surf. Sci. Catal.* **119**, 441–446 (1998).

54. López-Ortiz, A., Meléndez-Zaragoza, M. J., Salinas Gutiérrez, J. M., González-Vargas, P. E. & Collins-Martínez, V. Thermodynamic evaluation during the reduction of MWO4 (M = Fe, Mn, Ni) with methane for the production of hydrogen-syngas. *Int. J. Hydrogen Energy* **44**, 12315–12323 (2019).

55. Enger, B. r. C., Lødeng, R. L. & Holmen, A. Modified cobalt catalysts in the partial oxidation of methane at moderate temperatures. *J. Catal.* **262**, 188–198 (2009).